Fall 11-29-2011

In-situ Ellipsometry Characterization of Anodically Grown Silicon Dioxide and Lithium Intercalation into Silicon

Eric A. Montgomery
University of Nebraska-Lincoln, eric.montgomery@huskers.unl.edu

In-situ Ellipsometry Characterization of Anodically Grown Silicon Dioxide and Lithium Intercalation into Silicon

by

Eric Montgomery

A THESIS

Presented to the Faculty of
The Graduate College at the University of Nebraska
In Partial Fulfillment of Requirements
For the Degree of Master of Science

Major: Electrical Engineering

Under the Supervision of Professors Eva Schubert and Mathias Schubert

Lincoln, Nebraska

December 2011

In-situ Ellipsometry Characterization of Anodically Grown Silicon Dioxide and Lithium Intercalation into Silicon

Eric Montgomery, M.S.
University of Nebraska, 2011

Advisers: Eva Schubert and Mathias Schubert

In this thesis, in-situ ellipsometry and electroanalytical investigations of two electrochemical processes are reported: including the formation of anodically grown silicon dioxide and the intercalation of lithium-ions into silicon. Analysis of the ellipsometry data shows that the anodically grown silicon dioxide layer is uniform and has similar properties as thermally grown silicon dioxide. The lithium-ion intercalation data reveals non-uniform thin film formation, which requires further studies and development of appropriate ellipsometric optical models.

Acknowledgements

I would like to thank my advisors Dr. Eva Schubert and Dr. Mathias Schubert for their encouragement and support over the course of this work. I would also like to thank

- Dr. Natale Ianno for serving as a committee member and teacher.
- Dr. Tino Hofmann for his unbelievable patience while answering questions about everything under the moon.
- Dr. Tom Tiwald for his insight and discussion and the J.A. Woollam Co., Inc. for their instrument support.
- My colleagues Dr. Daniel Schmidt, Dr. Mario Saenger, Dr. Venkata Voora, Keith Rodenhausen, Stefan Schöche, Philipp Kühne, Alex Boosalis, Chad Briley, Charles Rice and Amitabha Sarkar.

Lastly I would like to thank my wife Elizabeth, my son Ethan and my parents Don and Nancy Montgomery, for their love, encouragement, support, and putting up with all my late nights and long lab hours. And an extra special thank you to my loving wife Elizabeth UMMS all the time.

Contents

List of Figures

List of Tables

Nomenclature

ϕ	sample in-plane (azimuthal) angle
φ, ψ, θ	Euler angles
AB-EMA	anisotropic Bruggeman effective medium approximation
CE	Counter Electrode
CPE	Constant-Phase Element
EC	Electrochemical Cell
EIS	Electrochemical Impedance Spectroscopy
EMA	Bruggeman effective medium approximation
NiCd	Nickel-Cadmium Battery
NiMH	Nickel-Metal-Hydride Battery
NiZn	Nickel-Zinc Battery
PLiON	Lithium-ion Polymer Battery
RE	Reference Electrode
SLI	Starting, lighting, ignition
WE	Working Electrode

Chapter 1

Introduction

Energy is a basic need of our economy. Therefore, the security of its supply is essential. This energy security is best supplied from domestic resources that are considered "green" or renewable, such as wind, solar, bio-fuels, *etc.* Though fossil fuel reserves are not yet depleted, they are unsustainable, possibly leading to an unstable economic future. The main focus of energy research today is to develop energy sources that are safe, affordable and renewable. Although there have been great advances in the ability to produce energy from renewable sources, the ability to store that energy has been lagging. Most renewable energies are highly variable and are not in sync with the peak power demand. It is therefore a challenge to store energy for times of peak demand. Currently, electric cars employ batteries that do not have enough energy capacity per cell. Batteries weigh too much, have issues with durability, safety concerns and a high cost. There is also an ever-increasing demand for better batteries for portable electronic devices that are smaller, lighter and have longer operation times.

Batteries that are lighter, have more energy, more power, and are longer lasting, rechargeable and durable are needed to solve our energy storage challenges.

Lithium batteries maybe the solution because they offer higher energy density, lighter weight and longer life spans than traditional electrochemical battery technologies. Silicon (Si) has been proposed as a new material for the use in lithium-ion (Li-ion) batteries and shows promise to meet the energy storage demands needed in the future. Si, theoretically, has the capability of storing 4.4 Li atoms per Si atom, giving Si a large theoretical specific capacity. This high specific capacity can cause a larger than 400% volume increase of Si that is potentially damaging, making the materials ability to recharge diminish quickly.

Recent studies of nanoscale materials in the form of thin films for Li-ion batteries are aimed at improving electrochemical performance of battery electrode materials and lowering their cost. These thin films have been shown to relieve the stress induced by intercalation (insertion) of Li-ions into the Si lattice, allowing efficient recharging for greater than 1000 cycles[3]. This thesis will study the challenges faced by intercalating of Li-ions into Si, and present two techniques, electrochemistry and ellipsometry, combined together to better understand the intercalation of Li into Si thin films.

Electrochemistry is a branch of chemistry that studies chemical reactions that take place in a solution at the interface of an electron conductor (a metal or a semiconductor) electrode and an ionic conductor (an electrolyte) and involve electron transfer between the electrode and the electrolyte or chemical species in solution. Using electrochemistry, one can apply electroanalytical techniques. The main electroanalytical techniques used here to study the electrochemical reactions are cyclic voltammetry, chronopotentiometry and electrochemical impedance spectroscopy (section 3.3). Each technique is carried out in an electrochemical (EC)

cell (see section 2.1.3) using a poteniostat or galvanostat (section 3.3). Each EC cell consists of a cathode electrode and an anode electrode that are separated by an electrolyte, which enables ionic transfer between the two electrodes. Once these electrodes are connected externally, chemical reactions proceed via the electrodes, electrons are driven and enable the current to be tapped by the user[4].

Ellipsometry is an optical technique using the reflection or transmission of polarized light to characterize thin films. Ellipsometry provides the complex refractive index, morphology, crystal quality, chemical composition and thickness from an optical model that is optimized using best-match models fit to experimental data sets.

Two electrochemical processes are investigated with combined electrochemistry and ellipsometry, the formation of silicon dioxide (SiO_2) via anodization and the intercalation of Li-ions into Si. Proof of concept for the combined technique is shown by verifying the well-known and understood thin film growth of anodically grown SiO_2. Then the controlled intercalation of Li-ions into silicon is investigated using the same combined electrochemistry and ellipsometry technique. The goal of this thesis is to gain insight into how to best improve the Li-ion intercalation into Si by using this combined technique.

1.0.1 Current Battery Technologies

A battery is composed of EC cells that are connected in series and/or in parallel to provide the required voltage and charge capacity. The voltage and charge capacity of a battery are functions of the materials they are made of. It is desirable that the amount of energy stored in a given mass or volume is as high as possible.

To compare the energy content of batteries, the terms gravimetric energy density (expressed in $\mathrm{W\,h\,kg^{-1}}$) and volumetric energy density (in $\mathrm{W\,h\,l^{-1}}$)[1] are used, whereas the rate capability is expressed as gravimetric power density (in $\mathrm{W\,kg^{-1}}$) and volumetric power density (in $\mathrm{W\,l^{-1}}$)[(4)]. One is naturally lead to search for materials that have a large number of free charge carriers per mass and volume per unit of a material.

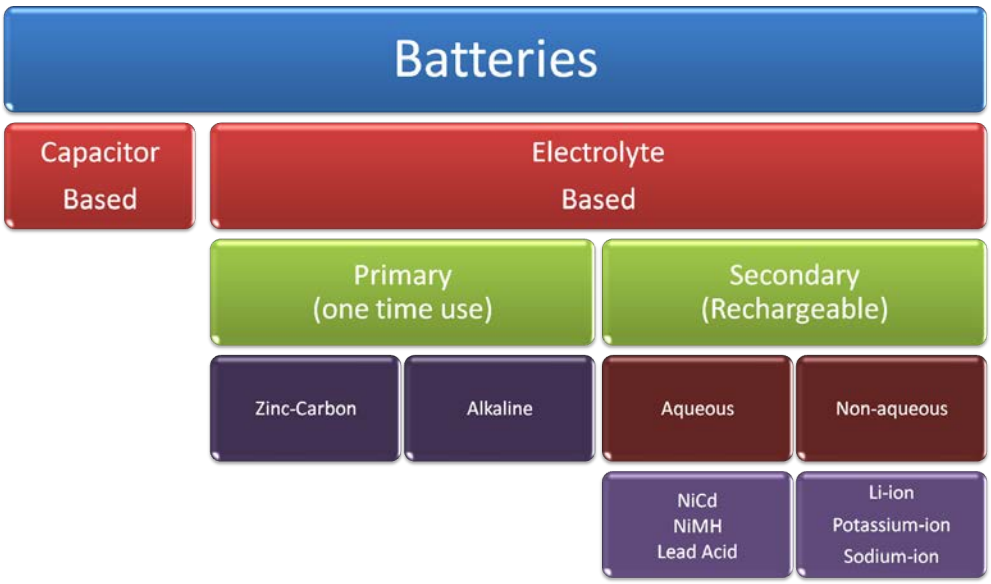

Figure 1.1: Basic categorization of battery types.

A basic categorization of battery types is depicted in Figure 1.1. Capacitive batteries rely on the formation of an electrical double layer and have some of the highest achievable power densities but also have low energy densities. These qualities make capacitive batteries excellent for energy storage where the battery

[1]The energy content of a battery is usually expressed indirectly by its capacity in ampere hours(A h); to convert watt hours (W h) to ampere hour (A h), the watt hour value must be divided by the voltage of the power source. This value is approximate since the voltage is not constant during discharge of a battery.

undergoes frequent charge and discharge cycles at high current and short duration. Electrolyte-based batteries are the most recognize as common batteries today. These can be split into primary (one time use) and secondary (rechargeable) batteries. Primary batteries have some of the highest gravimetric energy densities, but not necessarily large power densities. Primary batteries have high internal resistances that limit discharge to low current draw ($\leq 25\,\mathrm{mA}$) applications.

Secondary batteries can provide higher current densities for longer time periods. Secondary batteries can also be categorized into two groups that are dependent on the type of electrolyte used, either dissolved in aqueous or non-aqueous solvents (with or without water respectively). In aqueous batteries there is an exchange of one species for another; for example, in a Nickel-metal-hydride (NiMH) battery, at the negative electrode the chemical reaction is

$$\mathrm{H_2O + M + e^- \underset{Dis-charge}{\overset{Charge}{\rightleftharpoons}} OH^- + MH.}$$

The charge reaction is read left-to-right and the discharge right-to-left. For the forward charge reaction, the metal (M) gains a hydrogen bond while a water molecule is converted to a hydroxide ion. In non-aqueous batteries a species is inserted (intercalated) into the electrode; For example, in Lithium-cobalt batteries the negative electrode chemical reaction is

$$\mathrm{xLi^+ + xe^- + 6\,C \underset{Dis-charge}{\overset{Charge}{\rightleftharpoons}} Li_xC_6.}$$

Here during the charge reaction the Li-ion is intercalated into the carbon electrode by sharing electrons with the carbon (this process is colloquially known as plating or alloying the electrode).

Figure 1.2 shows how volume and gravimetric energy densities compare between the different rechargeable battery technologies available today. Lead acid batteries are mainly used for SLI (starting, lighting, ignition) in automobiles or standby applications such as uninterrupted power supplies. This is due to their capability to withstand extreme climate conditions, long life span, and cost-efficiency for SLI. Nickel-Cadmium (NiCd) batteries, which bear strong environmental concerns due to Cd-water contamination, are rarely seen today with the advent of the NiMH battery that is much safer, has higher energy density, and lower production costs than NiCd.

The Li-ion and Lithium-ion polymer battery (PLiON) are new contenders for the bulk share of the rechargeable battery market. They are currently in nearly every new portable electronic device from laptops to cell phones, and they are starting to overtake the portable power tool market replacing the widely used NiCd batteries. Although Li-ion batteries produce higher volumetric and gravimetric energy densities than their competitors in Figure 1.2, challenges still exist. For example when the battery is charged, deposits form inside the electrolyte that inhibit ion transport. Also these deposits can puncture the separator inside the battery, causing an electrical short and leading to thermal runaway and, possibly, combustion. Because of these safety concerns, almost all Li-ion batteries include internal circuitry to prevent failure conditions.

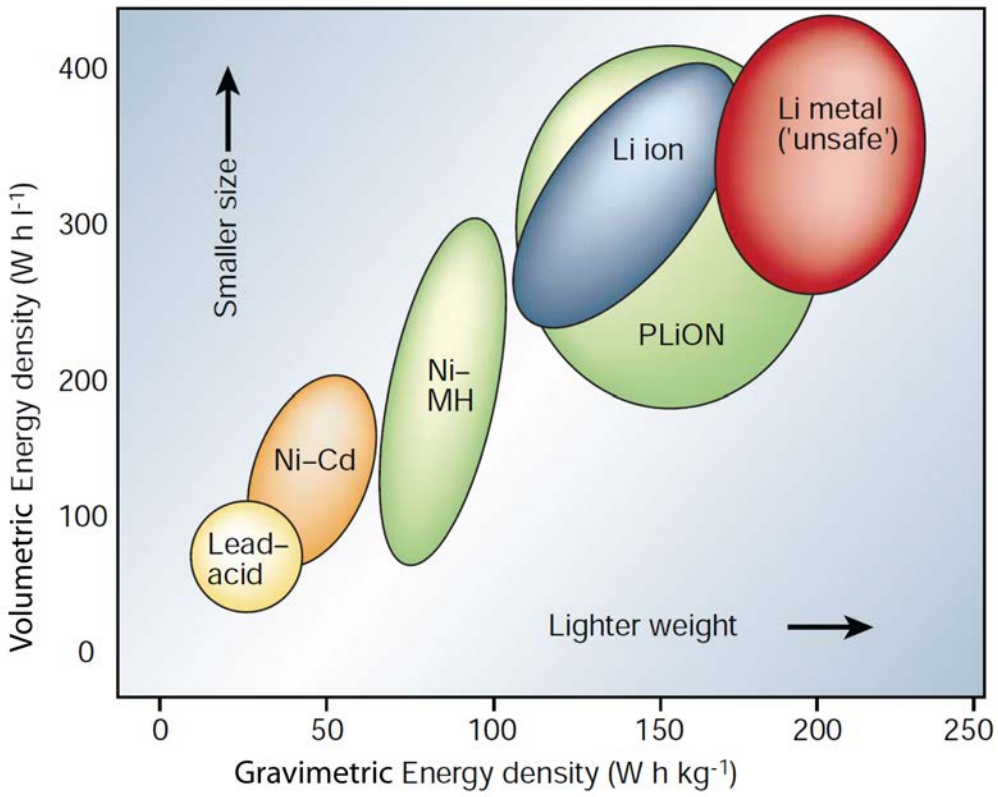

Figure 1.2: Comparison of the different battery technologies in terms of volumetric and gravimetric energy density. Adapted by permission from Macmillan Publishers Ltd: [Nature Publishing Group] (Tarascon and Armand), copyright (2001).

Chapter 2

Background and Motivation

2.1 Background

2.1.1 Silicon

Silicon (Si) is second only to oxygen as the most abundant element on Earth, at 27.7% of the earths crust[6]. Like diamond and other semiconductors from the Group IV elements, silicon crystallizes into the diamond crystal structure, where the lattice spacing for silicon is 0.543 071 0 nm (5.430 710 Å)[7]. Si has an atomic weight of 28.0855 amu, oxidation states of +2 and ±4, and a density of 2.33 g cm^{-3}. Silicon does not occur in a pure state in nature but is found in most rocks, clay and sand[8].

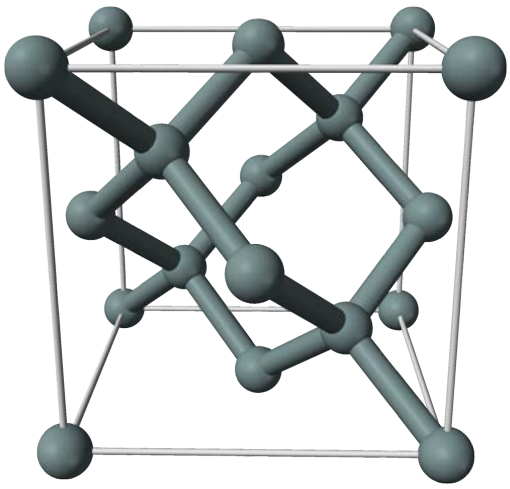

Figure 2.1: Silicon diamond lattice.

2.1.2 Lithium

Lithium (Li) ranks as the 33$^{\text{rd}}$ most abundant element on Earth[8]. It is a soft, white to silver metal that belongs to the Group I elements of the Periodic Table. Li has Atomic Number 3, oxidation states of ± 1 and a density of 0.534 $\mathrm{g\,cm^{-3}}$. The Group I metals are also known as the alkali metals and include sodium (Na), potassium (K), rubidium (Rb), caesium (Cs) and francium (Fr). Lithium has a single valance electron that is easily given up to form a positive ion (cation), see Figure **??**. This makes Li an excellent conductor for heat and electricity. Li is also the lightest metal in the periodic table. It would float on water but reacts violently with it, forming lithium hydroxide and highly flammable hydrogen as seen in Equation 2.1.

$$2\,\mathrm{Li(s)} + 2\,\mathrm{H_2O} \longrightarrow 2\,\mathrm{LiOH(aq)} + \mathrm{H_2(g)} \tag{2.1}$$

Lithium compounds such as lithium chloride, lithium carbonate, lithium phosphate, lithium fluoride and lithium hydroxide are more or less water soluble. For example, lithium hydroxide has a solubility of 129 $\mathrm{g\,l^{-1}}$.

2.1.3 Electrochemical Cell

An EC cell is capable of either creating electrical energy from chemical reactions, or driving chemical reactions through the introduction of electrical energy, for example, discharging or charging a battery. A battery is a type of galvanic cell that consists of two half-cells, each containing an electrode and electrolyte. In the EC cell electrons from one half-cell are lost (oxidation or anodic) to the respective electrode and species from the other half-cell gain electrons (reduction or cathodic) from the opposite electrode. If different electrolytes are used in each half-cell, a separator is used to isolate the two cells. The separator must still provide ionic conduction between the two electrolytes.

Each half-cell will have a characteristic voltage that varies depending on the choice of electrode and electrolyte and the undergoing equilibrium chemical reactions. Once the cell can provide no more energy to an external source, equilibrium is reached, and the cell can be charged again. The cell potential can be estimated using the difference between both half-cell electrode potentials.

An example of a galvanic cell is seen in Figure 2.2. In the cell there are two metals, zinc (Zn) and copper (Cu), both immersed in their corresponding metal sulfate aqueous solutions. Zn will be oxidized and Cu reduced. By definition, the Cu or reduced electrode is the cathode. The cathode is always the electrode that

gains electrons. Also by definition, the Zn or oxidized electrode is the anode.[1] The electrical potential for the cell can be calculated using a standard potential (E^0) table for the half-cells. Equations 2.2a and 2.2b represent the half-cell reactions and their half-cell standard potentials depicted in Figure 2.2. Equation 2.2c is the overall reaction of the cell. The cumulative standard potential for the cell will be $+0.34\,\mathrm{V} - (-0.76\,\mathrm{V}) = +1.10\,\mathrm{V}$.

$$\mathrm{Cu}^{2+} + 2\,\mathrm{e}^- \rightleftharpoons \mathrm{Cu} : \mathrm{E}^0 = +0.34\ \mathrm{V}, \tag{2.2a}$$

$$\mathrm{Zn}^{2+} + 2\,\mathrm{e}^- \rightleftharpoons \mathrm{Zn} : \mathrm{E}^0 = +0.76\ \mathrm{V}, \tag{2.2b}$$

$$\mathrm{Zn(s)} + \mathrm{Cu}^{+2} \longrightarrow \mathrm{Zn}^{+2} + \mathrm{Cu(s)}. \tag{2.2c}$$

2.1.4 Chemical Reactions of Batteries

Batteries are a galvanic cell, which is composed of two half-cells. A half-cell in its simplest form consists of a metal electrode partially immersed in a salt solution of the respective electrode metal. The salt solution contains cations of the

[1] A word of caution on nomenclature to readers: for the last 50 years, electrochemists have used the word "discharge" to mean the loss of positive electronic charge by combination with an electron, for example, if a hydrogen ion or proton is "discharged" it will become a hydrogen atom. If the ion is negatively charged, as in, Cl^-, the loss of an electron will normally be called discharge. On the other hand for the last 150 years, the addition of electrical energy to a cell has been called "electrical charging." So, battery researchers have called reductive reaction to a secondary cell electrode acting as an anode in the reverse direction, i.e, when the cell produces energy as "charging the anode." This nomenclature can become confusing quickly when reading scientific publications from different subsets of electrochemists or material scientists. If we take the example of Li insertion half-cells, $\mathrm{Li}^+ + \mathrm{e}^- \longrightarrow \mathrm{Li}_{\mathrm{substrate}}$, many will call the reaction a "discharge reaction" since the substrate is gaining negative Gibbs energy while it is electrically charged. But we are more interested in the amount of Li-ions a substrate is able to absorb and then release, reversibly, not the ability of Li^+ to combine with an electron. Therefore in this text we will use the term charging to represent the intercalation of Li^+ into Si.

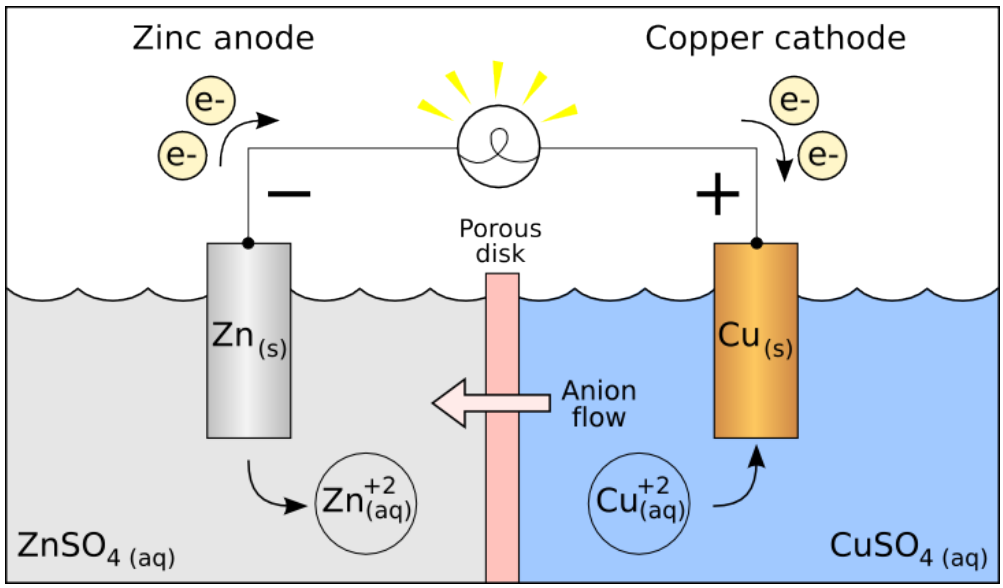

Figure 2.2: Galvanic cell based on the zinc-copper reaction. Made using two half-cells including the Zn(anode) electrode dipping into a Zn^{2+} solution and a Cu(cathode) electrode, which dips into a Cu^{2+} solution.

metal electrode which are ions with fewer electrons than protons, giving them net positive charges and anions that are ions with more protons than electrons giving them net negative charges to balance out the charge on the cations. Therefore the salt solution contains a metal in two oxidation states; the metal transitions between these states through what are called oxidation-reduction (redox) reactions. A redox reaction for a galvanic cell can be written symbolically as:

$$\text{Oxidation half-reaction} \qquad Y \longrightarrow X^+ + e^-, \tag{2.3a}$$

$$\text{Reduction half-reaction} \qquad e^- + Y^+ \longrightarrow X, \tag{2.3b}$$

$$\text{Overall (cell) reaction} \qquad X + Y^+ \longrightarrow X^+ + Y \tag{2.3c}$$

Equation 2.3c is analogous to equation 2.2c and describes the two half-cells in Figure 2.2. In this zinc-copper reaction, the two electrons generated in the oxidation of each Zn atom move through the Zn electrode and the wire and into the Cu electrode. From the Cu electrode the electrons reduce Cu^{2+} ions. Thus, electrons flow left to right through electrodes and wire[9].

The electrodes in the $ZnCu^{2+}$ cell are described as active because the metals, themselves, are components of the half-reactions. As the cell operates, the mass of the zinc electrode gradually decreases, and the amount of Zn^{2+} in the anode half-cell increases. At the same time, the mass of the copper electrode increases and the amount of Cu^{2+} in the cathode half-cell decreases[9]. **For many redox reactions, there are no reactants or products capable of serving as electrodes. In these cases, inactive electrodes are used.** The most commonly used are rods of graphite or platinum. These electrodes conduct electrons but are ideally chemically inert during the half-reactions.

2.2 Motivation

Li-ion battery cells are currently most widely used as rechargeable batteries for consumer electronics and show promise for use in electric/hybrid vehicles. Other conventional aqueous rechargeable batteries, such as NiCd and NiMH, have lower energy densities, lower operating voltages, higher self-discharge, and higher maintenance requirements than Li-ion batteries[3]. These qualities make Li-ion batteries some of the highest performing batteries available. Since our consumer electronics, military, aerospace, and automobile applications require the miniaturization of their components, Li-ion cells still need higher volumetric energy capacities to give the battery a smaller overall size, and gravimetric energy densities to make the battery last longer.

Lithium can be electrochemically intercalated into a number of metals at room temperature, for example, Sn, Pb, Al, Au, Pt, Zn, Cd, Ag and Mg. But this process usually results in irreversible damage to the electrodes and loss of electronic contact. Intercalation and de-intercalation into Si has been shown to be reversible at high temperatures and can result in the formation of $Li_{12}Si_7$, $Li_{14}Si_6$, $Li_{13}Si_4$ or $Li_{22}Si_5$ alloys[2,3]. The alloying state of $Li_{22}Si_5$ corresponds to 4.4 Li atoms per Si atom, leading to a specific intercalation capacity of $4200\,\mathrm{mA\,h\,g^{-1}}$. This high specific capacity makes Si an attractive material for use as an anode in Li-ion batteries. However, volume expansion/contraction processes at room temperature causes Si to lose reversibility through many intercalation/de-intercalation cycles.

Li insertion into Si yields successive LiSi alloys, each of which results in progressively larger volume expansions of the parent lattice. Table 2.1 shows the data for crystal structure, unit cell volume, and volume per silicon atom for each alloy

formed during the alloying process. It shows that the volume per silicon atom for $Li_{22}Si_5$ alloy is four times higher than that of the parent silicon atom [2,3].

Table 2.1: Crystal structure, unit cell volume and volume per Si atom for the Li-Si system [2,3].

Compound and crystal structure	Unit cell volume($Å^3$)	Volume per silicon atom($Å^3$)	Theoretical density ($g\,cm^{-3}$)
Silicon cubic	160.2	20.0	2.33
$Li_{12}Si_7$, ($Li_{1.71}Si$) orthorhombic	243.6	58.0	1.15
$Li_{14}Si_6$, ($Li_{1.71}Si$) rhombohedral	308.9	51.5	1.43
$Li_{13}Si_4$, ($Li_{3.25}Si$) orthorhombic	538.4	67.3	1.38
$Li_{22}Si_5$, ($Li_{4.4}Si$) cubic	659.2	82.4	1.18

In early research of Li-ion intercalation into Si it was believed that the low coulombic efficiency[1] of bulk Si was caused by low electrochemical reactivity of the Li with Si at room temperature. However, the results from intercalation/de-intercalation cycling show that low coulombic efficiency is due to electrode cracking and disintegration from the large volumetric expansion, causing the electronic contact to the current collector (metal contact to Si anode) to be diminished. A scanning electron microscope (SEM) image of this stress-induced cracking can be seen in Figure 2.3. To overcome this volumetric expansion induced cracking, many techniques have been employed to relieve the stress induced by the Si lattice upon intercalation. Examples include the use of Si micro- to nano-scale structured

[1]Coulombic losses are experienced by both electrolytic and galvanic cells. These losses are usually in the form of misdirected electrons which participate in unproductive reactions, product recombination, a short circuit the system, and other diversions for electrons. These losses are physically expressed in the system as heat and sometimes chemical byproducts.

anodes, Si coated with materials such as carbon, carbon nano-tubes coated with Si and Si thin films (thickness<500 nm).

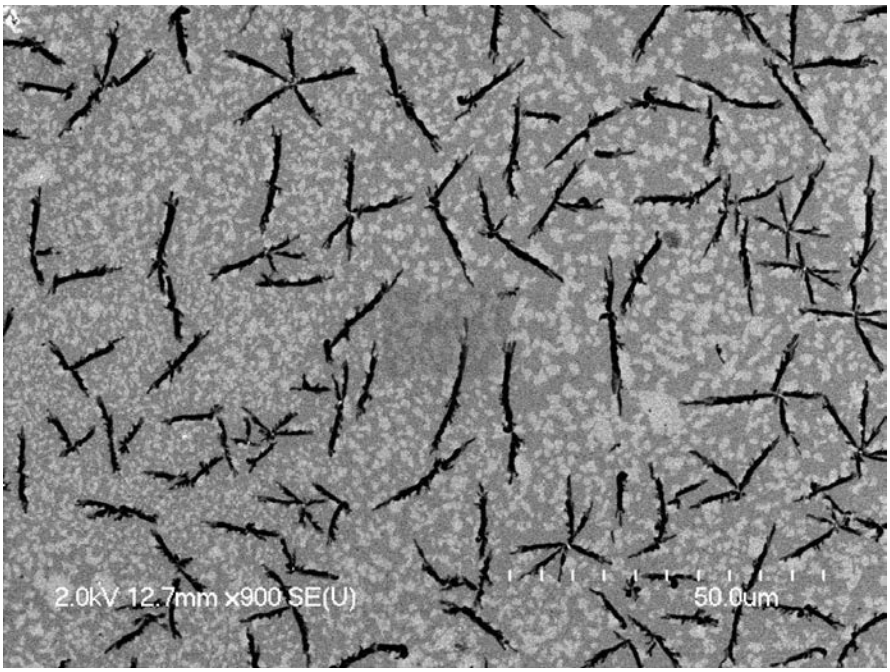

Figure 2.3: SEM image of amorphous silicon thin film with a thickness of 200 nm after 15 intercalation/deintercalation cycles, showing the stress-induced cracking from the volumetric expansion of the Si film (see section 5.2.2).

Chapter 3

Characterization Techniques

3.1 Spectroscopic Ellipsometry

3.1.1 Standard Spectroscopic Ellipsometry

Ellipsometry is an optical technique that characterizes light, after reflection or transmission from a sample[10]. Using polarized light ellipsometry measures the change in polarization upon light interaction with a sample. The name ellipsometry comes from the fact that polarized light often becomes elliptically polarized upon sample reflection. Ellipsometry measures the two independent ellipsometric real valued parameters Ψ and Δ, which depend on the ratio of the complex-valued Fresnel refection coefficients for the polarizations perpendicular (s) and parallel (p) to the plane of incidence (figure 3.1).

Standard spectroscopic ellipsometry can be applied when neither s- or p-polarized light is converted into the other upon reflection from a sample. This is the case for optically isotropic samples, such as amorphous materials. The standard ellipsometric parameters are defined through Ψ and Δ. They are related to the complex reflectance ratio ρ as a function of the Fresnel reflection coefficients

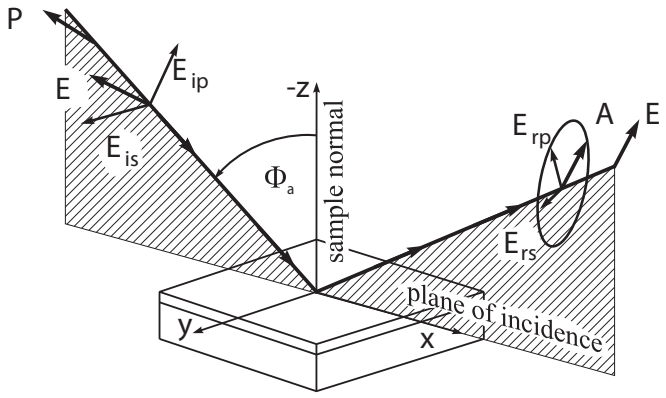

Figure 3.1: The wave vector of the incident and emerging plane waves (reflected at and angle Φ_a) and the normal to the sample surface define the plane of incidence. The complex plane wave amplitudes of the p-polarized and s-polarized modes before and after reflection from the sample are denoted by E_{ip}, E_{is}, and E_{rp}, E_{rs}, respectively. P and A are the azimuth angles of the linear polarizers used, for example, in the standard arrangement of rotating analyzer (polarizer) ellipsometers.

(R_p, R_s) of the sample, defined as:

$$\rho \equiv \left(\frac{E_{rp}}{E_{ip}}\right) \Big/ \left(\frac{E_{rs}}{E_{is}}\right) \equiv \frac{R_p}{R_s} \equiv \tan\Psi e^{(\mathrm{i}\Delta)}. \tag{3.1}$$

As shown in figure 3.1, ellipsometry measures the two values (Ψ, Δ) that express the amplitude ratio and phase difference between p- and s-polarizations, respectively. In ellipsometry, therefore, the variation of light reflection with p- and s-polarizations is measured as the change in polarization state. In particular, when a sample structure is simple, the amplitude ratio Ψ is characterized by the refractive index n, while Δ represents light absorption described by the extinction coefficient k. In this case, the two values (n,k) can be determined directly from the two ellipsometry parameters (Ψ, Δ) obtained from a measurement by applying the Fresnel equations. This is the basic principle of ellipsometry measurement[10].

Data can be displayed as Ψ and Δ, or the pseudo-dielectric function ($\langle\varepsilon\rangle$), which is direct inversion of the ellipsometric Ψ and Δ data, measured at the angle Φ_a, Where one assumes bulk behavior for the sample investigated. The ambient-substrate model relates the pseudo substrate dielectric function with the ellipsometric parameters[11].

$$\langle\varepsilon\rangle = \varepsilon = \sin{\Phi_a}^2 \left[1 + \tan{\Phi_a}^2 \left(\frac{1-\rho}{1+\rho}\right)^2\right]. \tag{3.2}$$

The pseudo substrate is commonly used if the surface overlayer effects are negligible and the actual substrate ε is comparable with $\langle\varepsilon\rangle$.

3.1.2 Definition of the refractive index

The ellipsometric quantities Ψ and Δ are related to wave optics through a solution of the wave equation: $\mathbf{E} = E_0\exp\{\mathrm{i}\mathbf{kr}\}$, with E_0 being the amplitude of the

electric-field intensity $\mathbf{E}$ at spatial variable $\mathbf{r}$. The propagation vector $\mathbf{k}$ is a function of the complex valued refractive index of the medium $N = n + \imath k$. The refractive index n follows experimentally from Snell's law[12]:

$$n_1 \sin\theta_1 = n_2 \sin\theta_2, \tag{3.3}$$

where θ_j is the angle of incidence counted toward the interface between the two materials with index of refraction n_1 and n_2. The extinction coefficient k is connected to the absorption, measured by intensity ($I = \mathbf{E}\mathbf{E}^*$) loss upon wave propagation over a distance d,

$$I = I_0 e^{-\alpha' d}, \tag{3.4}$$

with the absorption coefficient α' being

$$\alpha' = \frac{4\pi}{\lambda} k. \tag{3.5}$$

3.1.3 Jones Matrix Representation

The complex ratio ρ can be approached by using different representations of the electromagnetic plane wave response. If a sample is anisotropic, which causes mode conversion between p- and s-polarized light upon reflection (or transmission), one must expand the number of parameters used to describe the plane wave response. For non-depolarizing samples the Jones matrix representation provides complete mathematical description for the electromagnetic plane wave response.

The Jones reflection matrix $\mathbf{J}$, relates the incident A modes (p,s) with emerging B plane wave modes (p,s):

$$\begin{pmatrix} B_p \\ B_s \end{pmatrix} = \mathbf{J} \begin{pmatrix} A_p \\ A_s \end{pmatrix} = \begin{bmatrix} r_{pp} & r_{ps} \\ r_{sp} & r_{ss} \end{bmatrix} \begin{pmatrix} A_p \\ A_s \end{pmatrix}. \tag{3.6}$$

The Jones matrix **J** contains the four, so called, anisotropic Fresnel reflection coefficients $(r_{pp}, r_{ps}, r_{sp}, r_{ss})$.[1] If the optical system is a mode converting system the off-diagonal elements (r_{ps}) and (r_{sp}) of **J** will be nonzero.

3.1.4 Mueller Matrix Representation

If a sample introduces depolarization the Mueller matrix scheme can represent both partially polarized light but also includes depolarization phenomena. The Mueller matrix representation uses the Stokes vector formalism, which are four real-valued Stokes parameters $(S_j, j = 0..3)$ of an electromagnetic plane wave. These four parameters are defined by the $p-$ and $s-$polarized coordinate system:

$$S_0 = I_p + I_s, \tag{3.7a}$$

$$S_1 = I_p - I_s, \tag{3.7b}$$

$$S_2 = I_{(45)} - I_{(-45)}, \tag{3.7c}$$

$$S_3 = I_{(\sigma+)} + I_{(\sigma-)}. \tag{3.7d}$$

where I_p, I_s, I_{-45}, I_{45}, $I_{\sigma+}$ and $I_{\sigma-}$ are the intensities for the $p-$, $s-$, $+45°$, $-45°$, right- and left-handed circularly polarized light components, respectively[(13)].

Depolarization is the reduction of the degree of polarization of light[(14)]. In the Mueller representation depolarization can be pictured as a coupling of polarized into unpolarized light, where polarized light is incident and the exiting Stokes vector can be expressed by the Stokes parameters as

$$D_p = \frac{I_{pol}}{I_{tot}} = \frac{(S_1^2 + S_2^2 + S_3^2)^{1/2}}{S_0}, \qquad 0 \leq D_p \leq 1, \tag{3.8}$$

[1] In this notation the first index is the incident polarization mode and the second index is the outgoing polarization mode.

where I_{tot} is the total intensity of the input beam and I_{pol} is the sum of the intensity of the polarization components. When $D_p = 1$, $D_p = 0$ or $0 < D_p < 1$ this represents completely polarized, unpolarized or partially polarized light respectively. The Mueller matrix is a 4 x 4 matrix with real-valued elements[14]. For a polarizing sample the Mueller matrix ($\mathbf{M}$) is defined as a matrix which transforms an incident Stokes vector ($\mathbf{S}_{\text{in}}$) into the exiting Stokes vector ($\mathbf{S}_{\text{out}}$),

$$\mathbf{S}_{\text{out}} = \mathbf{M} \bullet \mathbf{S}_{\text{in}} = \begin{pmatrix} M_{11} & M_{12} & M_{13} & M_{14} \\ M_{21} & M_{22} & M_{23} & M_{24} \\ M_{31} & M_{32} & M_{33} & M_{34} \\ M_{41} & M_{42} & M_{43} & M_{44} \end{pmatrix} \begin{pmatrix} S_0 \\ S_1 \\ S_2 \\ S_3 \end{pmatrix}_{\text{in}} = \begin{pmatrix} S_0 \\ S_1 \\ S_2 \\ S_3 \end{pmatrix}_{\text{out}} . \tag{3.9}$$

3.1.5 Generalized Ellipsometry

When Ψ and Δ depend on the polarization state of the incident electromagnetic plane wave, generalized ellipsometry can be used. This concept is for both the Jones and Mueller matrix formalisms. Using the Jones matrix representation six real-valued generalized ellipsometry angles Φ_{ij} and Δ_{ij} are defined by the three ratios of the four available complex-valued elements of the Jones reflection matrix $\mathbf{J}$[12,15,16]:

$$R_{pp} \equiv \frac{r_{pp}}{r_{ss}} = \tan \Psi_{pp} \exp\left(\imath \Delta_{pp}\right), \tag{3.10a}$$

$$R_{ps} \equiv \frac{r_{ps}}{r_{ss}} = \tan \Psi_{ps} \exp\left(\imath \Delta_{ps}\right), \tag{3.10b}$$

$$R_{sp} \equiv \frac{r_{sp}}{r_{pp}} = \tan \Psi_{sp} \exp\left(\imath \Delta_{sp}\right). \tag{3.10c}$$

The use of generalized ellipsometry is required when the optical system response is anisotropic. The anisotropy results in non-zero off-diagonal elements of the Jones and Mueller matrices[12,15,16].

3.1.6 Representation of the Dielectric Function

The refractive index of certain media may be different depending on the polarization and direction of propagation of the light through the medium, this is known as birefringence or anisotropy. In materials with non-cubic symmetry, the dielectric constant can be described by a rank-2 tensor ε, expressed in Cartesian coordinates(x, y, z):

$$\mathbf{D} = \varepsilon_0(\mathbf{E} + \mathbf{P}) = \varepsilon_0\varepsilon\mathbf{E} = \varepsilon_0 \begin{pmatrix} \varepsilon_{xx} & \varepsilon_{xy} & \varepsilon_{xz} \\ \varepsilon_{yx} & \varepsilon_{yy} & \varepsilon_{yz} \\ \varepsilon_{zx} & \varepsilon_{zy} & \varepsilon_{zz} \end{pmatrix} \mathbf{E}, \tag{3.11}$$

where vectors $\mathbf{D}$, $\mathbf{P}$ and $\mathbf{E}$ are the electric displacement field, dielectric polarization density and electric field respectively along the unit directions $\mathbf{x}$, $\mathbf{y}$ and $\mathbf{z}$. And ε_0 is the vacuum permittivity.

$$\mathbf{D} = \mathbf{x}D_x + \mathbf{y}D_y + \mathbf{z}D_z, \tag{3.12a}$$

$$\mathbf{E} = \mathbf{x}E_x + \mathbf{y}E_y + \mathbf{z}E_z, \tag{3.12b}$$

$$\mathbf{P} = \mathbf{x}P_x + \mathbf{y}P_y + \mathbf{z}P_z. \tag{3.12c}$$

Generally, the dielectric function tensor ε is a function of $\hbar\omega$ due to non-local response within the time domain (frequency dispersion). For mediums without spatial mirror (chiral) symmetry (optically active mediums), ε depends on the photon wave vector $\hbar k$[11].

3.1.7 Orthogonal Rotations

Orthogonal rotations relate the sample and the laboratory Cartesian coordinate axes. To properly address the ε tensor, we let the plane of incidence (x, z) and

the sample surface (x, y) with the origin at the sample surface all be set in a right-handed (x, y, z) Cartesian system. Using the (real-valued) Euler angles φ, ψ and θ, one can rotate between the laboratory (x, y, z) and the Cartesian crystal coordinate system (ξ, η, ζ) as seen in Figure 3.2.

$$\varepsilon(x, y, z) = \mathbf{A}\varepsilon(\xi, \eta, \zeta)\mathbf{A}^{-1}, \tag{3.13}$$

where the unitary matrix $\mathbf{A}$ is the orthogonal rotation matrix[11]

$$\begin{pmatrix} \cos\psi\cos\varphi - \cos\theta\sin\varphi\sin\psi & \cos\psi\sin\varphi + \cos\theta\cos\varphi\sin\psi & \sin\psi\sin\theta \\ -\cos\psi\sin\varphi + \cos\theta\sin\varphi\sin\psi & -\sin\psi\sin\varphi + \cos\theta\cos\varphi\cos\psi & \cos\psi\sin\theta \\ \sin\theta\sin\psi & -\sin\theta\cos\varphi & \cos\theta \end{pmatrix}. \tag{3.14}$$

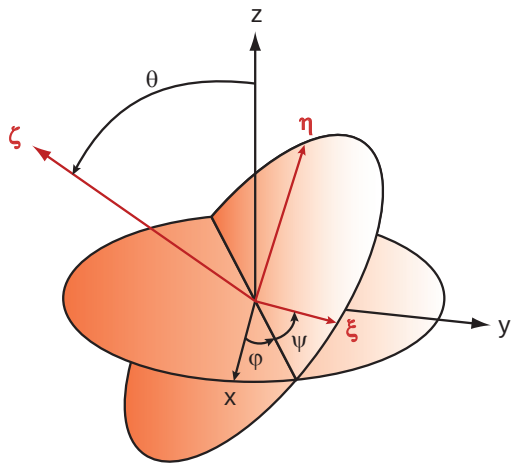

Figure 3.2: Definition of the Euler angles φ, ψ and θ and the orthogonal rotations as provided by $\mathbf{A}$. (ξ, η, ζ) and (x, y, z) refer to the Cartesian auxiliary and laboratory coordinate systems, respectively.

3.1.8 Analysis and Modeling

Ellipsometry is an indirect measurement method. Only in the special case of a bulk sample can the experimental data can be transformed directly into the dielectric function. In all other cases the experimental data have to be analyzed by point-by-point fitting algorithms or a line shape analysis using analytical dielectric function models. For the ellipsometric data analysis the dielectric function(s) and thickness for all relevant sample constituents of a layered sample structure have to be considered in the model calculations. Model parameters are then varied until the experimental and modeled data match as close as possible[17]. Different dielectric function models are used for different spectral regions.

For dielectric function modeling in a transparent spectral region ($\varepsilon_2 \backsim 0$), the Sellmeier or Cauchy model is used. In spectral regions with free-carrier absorption or lattice absorption, the data analysis is generally performed using Lorentz oscillator models. The dielectric function based on a Lorentz oscillator can be described by:

$$\varepsilon = 1 + \frac{e^2 N_e}{\varepsilon_0 m_e} \frac{1}{(\omega_0^2 - \omega^2) + \imath\Gamma\omega}, \tag{3.15}$$

where N_e is the number of electrons per unit volume, m_e and e are the mass and charge of the electron, respectively, ω_0 is the resonance frequency for the atomic oscillator and Γ is the damping coefficient. Using Equation 3.15 in a region where ($\varepsilon_2 \backsim 0$) and assuming $\Gamma \to 0$ at $\omega \lll \omega_0$ and substituting $\omega/c = 2\pi/\lambda$, where λ is the wavelength, we obtain the Sellmeier Equation:

$$\varepsilon = \varepsilon_1 = 1 + \frac{e^2 N_e}{\varepsilon_0 m_e (2\pi c)^2} \frac{\lambda_0^2 \lambda^2}{\lambda^2 - \lambda_0^2}. \tag{3.16}$$

Examining the Equation note that ($\varepsilon_2 = k = 0$ when $\Gamma = 0$), and the Sellmeier model can be rewritten into the form:

$$\varepsilon_1 = n^2 = A + \sum_j \frac{B_j \lambda^2}{\lambda^2 - \lambda_{0j}^2}, \quad \varepsilon_2 = 0, \tag{3.17}$$

where n is the refractive index, A and B_j represent analytical parameters used in data analysis and λ_0 corresponds to ω_0.

In most cases a two term Sellmeier model is adequate to account for UV and IR absorption. The representation of the two term Sellmeier model index of refraction is:

$$n = \sqrt{\varepsilon(\infty) + \frac{A\lambda^2}{\lambda^2 - B^2} - E\lambda^2}, \tag{3.18}$$

where $\varepsilon(\infty)$ is an index offset, A is the amplitude, B is the center energy and E is the position of a pole in the infrared.

3.1.9 Bruggeman Effective Medium Approximation

The Bruggeman effective medium approximations (EMA) are physical models based on homogenous mixing of two or more materials. Spherical geometry is assumed, so that if N isotropic phases, with permittivities ε_j, form a mixture, each occupying a volume fraction f_j with $\sum_{j=1}^{N} f_{j=1}$, and the consistency requirement for the effective permittivity ϵ_{eff} of the mixed conducting matrix is

$$\sum_{j=1}^{N} f_j \frac{\varepsilon_j - \varepsilon_{eff}}{\varepsilon_j + 2\varepsilon_{eff}} = 0. \tag{3.19}$$

The mixing rule for an ordinary two-phase matrix, the Bruggeman formula is

$$(1 - f)\frac{\varepsilon_e - \varepsilon_{eff}}{\varepsilon_e + 2\varepsilon_{eff}} + f\frac{\varepsilon_i - \varepsilon_{eff}}{\varepsilon_i + 2\varepsilon_{eff}} = 0, \tag{3.20}$$

where spherical inclusions (ε_i) are with volume fraction f, are in the homogeneous environment (ε_e).

3.1.10 Anisotropic Bruggeman Effective Medium Approximation

For the case when the Bruggeman EMA is formulated assuming randomly oriented ellipsoids it is represented by

$$\varepsilon_{eff} = \varepsilon_e + \frac{f}{3}(\varepsilon_i - \varepsilon_e) \sum_{j=x,y,z} \frac{\varepsilon_{eff}}{\varepsilon_{eff} + N_j(\varepsilon_i - \varepsilon_{eff})}, \tag{3.21}$$

where N_j are the depolarization factors of the inclusion ellipsoids along the three orthogonal major polarizability axes as seen in figure (1a,c), with volume fraction f, located in homogeneous environment ε_e.

This approach can also be applied to highly ordered inclusions; namely the anisotropic Bruggeman EMA (AB-EMA). Depolarization factors L_x^D, L_y^D, and L_z^D are used to represent the relative polarizability dimensions of elliptical inclusion along the major polarizable axes x, y and z, (see Figure 3.3). When these inclusions are aligned in a host matrix the biaxial effective dielectric functions $\varepsilon_{eff,x}$, $\varepsilon_{eff,y}$, and $\varepsilon_{eff,z}$ are used along the polarization axes x, y, and z respectively. The AB-EMA formulas for the three effective dielectric functions are then:

$$f\frac{\varepsilon_i - \varepsilon_{eff,j}}{\varepsilon_{eff,j} + L_j^D(\varepsilon_i - \varepsilon_{eff,j})} + (1-f)\frac{\varepsilon_e - \varepsilon_{eff,j}}{\varepsilon_e + 2\varepsilon_{eff,j}} = 0, \qquad j = x, y, z, \tag{3.22}$$

where ε_i and ε_e are the dielectric functions of the respective bulk materials used in the matrix. The polarization factors L_j^D must sum to unity:

$$1 = L_x^D + L_y^D + L_z^D \tag{3.23}$$

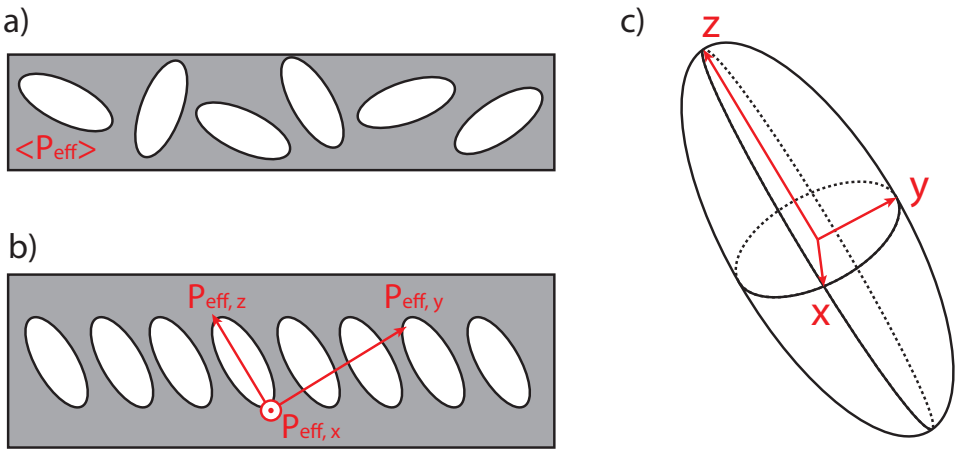

Figure 3.3: Effective medium approximations EMA, AB-EMA, and elliptical inclusions (a), (b), and (c) respectively. (a) Exhibits an average effective polarizability $\langle \mathbf{P}_{eff} \rangle$. (b) Shows anisotropic properties and has three effective polarizabilites $\mathbf{P}_{eff,j}$ that will change according to the shape of inclusions.

3.2 Simulations

In this section simulations to demonstrate the capability of ellipsometric measurement techniques are presented. These simulations of Li intercalation into highly ordered 3D nano-structured *a*-Si thin films are preformed using V.A.S.E software from the J.A Woollam Co. A model was constructed using the AB-EMA model to show how the different parameters will change the Mueller matrix (MM) elements. The main function of these simulations is to find the largest change in the MM elements vs. percentage of Li intercalation into Si; since only one angle can be taken through the EC cell one must choose the in-plane orientation of the sample carefully to maximize the effectiveness of each measurement.

The AB-EMA contains three constituents *a*-Si, Li and void fraction with a

layer thickness of 100 nm. Tabulated optical constants for a-Si from Palik et al.[18] and Li from Rasigni and Rasigni[19] were used in all calculations. In Figure 3.4 the Euler angles and percentage of constituents is held constant (a-Si = 17.5%, void = 30%, Li = 52.5%), while the sample is rotated in-plane from $\phi = 0 - 360°$. This simulation shows that the AB-EMA has mirror or translational symmetry at 180°, therefore, all simulations following will be varied from $\phi = 0 - 180°$. The AB-EMA also exhibits two pseudo-isotropic orientations, which occur when the slanting plane is parallel to the plane of incidence ($\phi = 0°, 180°$)[12].

The next set of simulations (Figure 3.5) seek to find the in-plane orientation that will show the largest changes over time in the MM elements (or change in Li versus a-Si). To accomplish this the Euler angle φ is changed to 45°, 90°, 135°, and 180° (this is equivalent to rotating the sample in-plane). And keeping the remaining Euler angles at $\theta = 65°$ and $\psi = 0°$. The simulation uses starting parameters of 30% a-Si, 0% Li and 70% void fraction. Li and void fraction were then linearly varied from there starting point to 70% and 0% respectively over a 60 min period. The starting value for each Mueller matrix element is then subtracted from subsequent data points to better show change over time.

Figure 3.5 shows all four simulations of the different in-plane angles, it is clear from this plot that at both 45° and 135° in-plane orientations the largest change over time in all MM elements with the exception of M_{33} can be seen. It can also be seen in Figure 3.5 that the anisotropic MM off diagonal elements (M_{kl} and M_{lk} with $k = 1, 2; l = 3; 4$) that represent the off diagonal Jones matrix elements show much larger changes since they do not fall close to the pseudo-isotropic points.

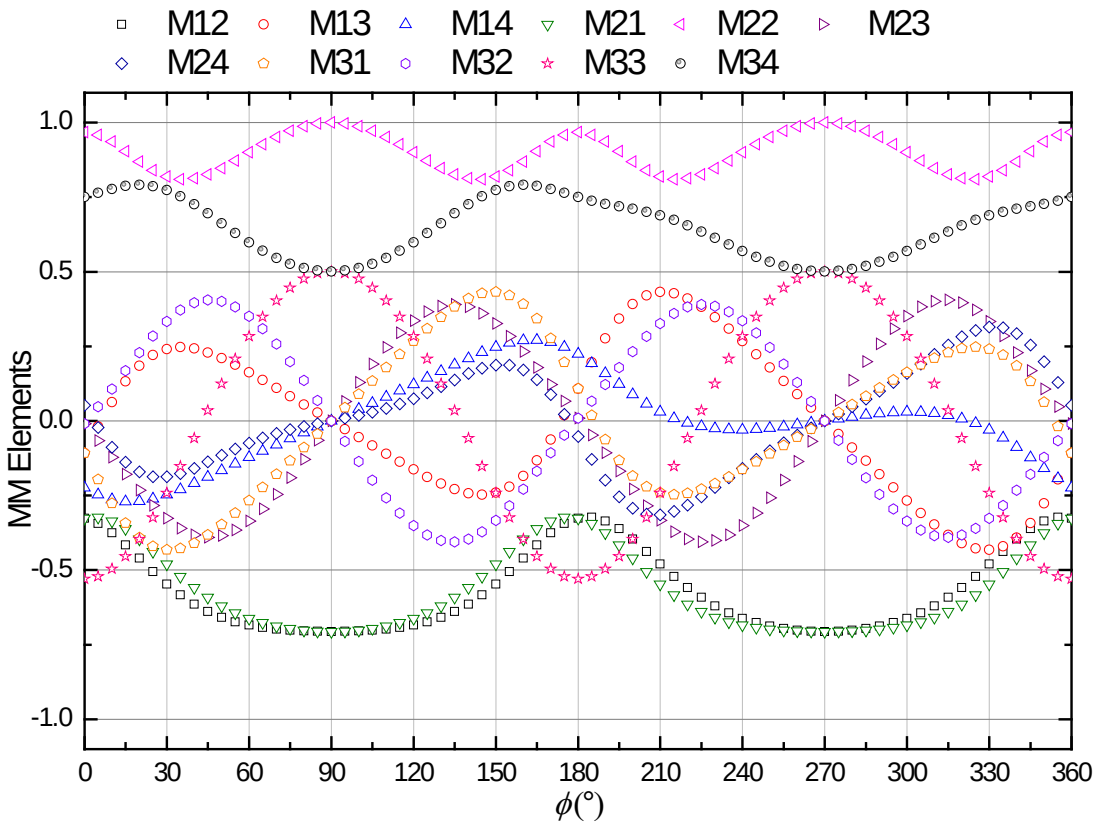

Figure 3.4: Three constituent AB-EMA simulation of Mueller matrix elements using Euler angles of $\varphi = 0°$, $\theta = 65°$ and $\psi = 0°$ while percentage of constituents is held constant (a-Si = 17.5%, void = 30%, Li = 52.5%) and then rotating the sample in-plane from $\phi = 0° - 360°$. This simulation shows that the AB-EMA has mirror or translational symmetry at 180°, and also exhibits two pseudo-isotropic orientations, which occur when the slanting plane is parallel to the plane of incidence ($\phi = 0°, 180°$)

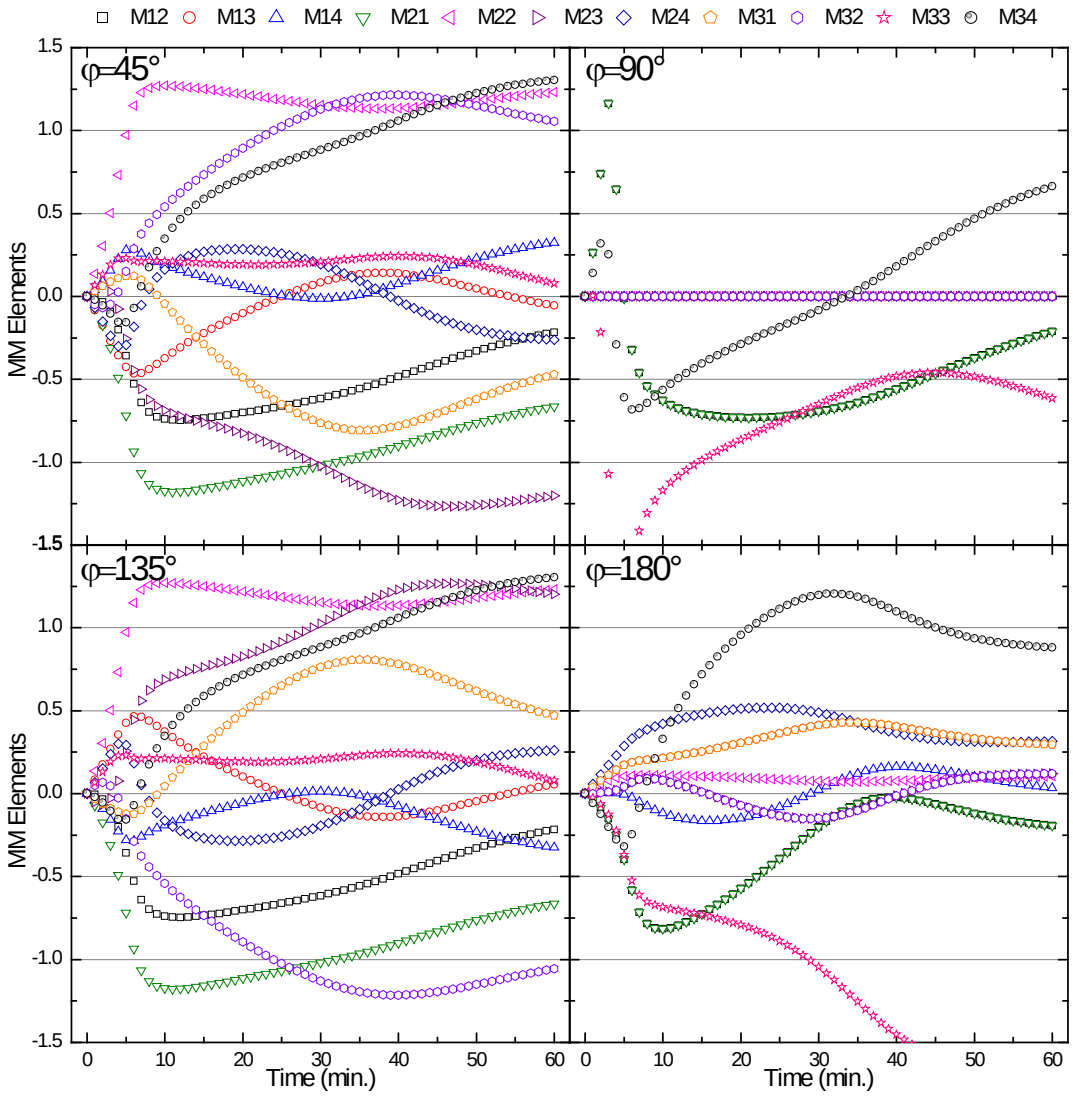

Figure 3.5: Model simulation of Mueller matrix elements using Euler angles of $\varphi = 45°, 90°, 135°, 180°$, $\theta = 65°$ and $\psi = 0°$ while varying Li and void percentage vs. time. Over 60 min void and Li are linearly changed from 70 to 0% and 0 to 70% respectively.

3.3 Electroanalytical Techniques

3.3.1 Electrochemical Setup

Electroanalytical experiments use a potentiostat or galvanostat, where a potentiostat will apply a voltage and measures the current and a galvanostat applies a current and measures the voltage. In this work a three-electrode system, consisting of a working electrode (WE), counter electrode (CE) and reference electrode (RE) is incorporated into a half-cell. In this arrangement, the current is passed between the WE and the CE. The CE electrode can be of any convenient material, because its electrochemical properties do not affect the behavior of the electrode of interest. The CE is usually chosen such that it does not produce chemical products by electrolysis that may potentially cause interfering reactions at the WE surface[1]. The RE is a self contained half-cell with a stable and well-known electrode potential. Its only role is to act as reference in measuring and controlling the working electrode potential and does not pass any current. The three-electrode system is shown schematically in Figure 3.6.

The RE is the most complex of the three electrodes. There are a variety of standard RE electrodes that are compatible with different cell material constructions. The most commonly used RE is the silver-silver chloride electrode ($Ag/AgCl^-$). A silver chloride RE has an overall half-cell reaction of $Ag(s) + Cl^- \longleftrightarrow AgCl(s) + e^-$ and has a standard potential that varies depending on the filling solution concentration (see table 3.1). The $Ag/AgCl^-$ reference electrode is employed in this work. The potential (ϕ) drop across the electrolyte solution can be compensated if a three-electrode system is used, where $\phi_{ref} = \phi_{\mathrm{WE}} - \phi_{\mathrm{CE}}$. Consider the potential

Table 3.1: Standard Potentials for silver -silver chloride reference electrode[(1)]

Electrode	Potential (E^0) mV
SHE	0
Ag/AgCl/Sat. KCl	199
Ag/AgCl/3.5M KCl	205
Ag/AgCl/0.1M KCl	288
Ag/AgCl/Sat. NaCl	197

profile in solution between the working and auxiliary electrodes, shown in Figure 3.7. The solution between the electrodes can be represented by a potentiometer. But even in this arrangement, not all iR_s can be compensated. Where i is the applied current and R_s is the resistance of the solution. If the reference electrode is placed anywhere but exactly at the electrode surface, some fraction of the potential drop will be included in the measured potential, called iR_u, where R_u is the uncompensated resistance. Consequently, when modeling data one must account for iR_u, which can easily be measured using the electrochemical impedance technique described in section 3.3.4.[1]

[1]The equipment used in all experiments in this work includes circuitry for electronic compensation of the iR_u.

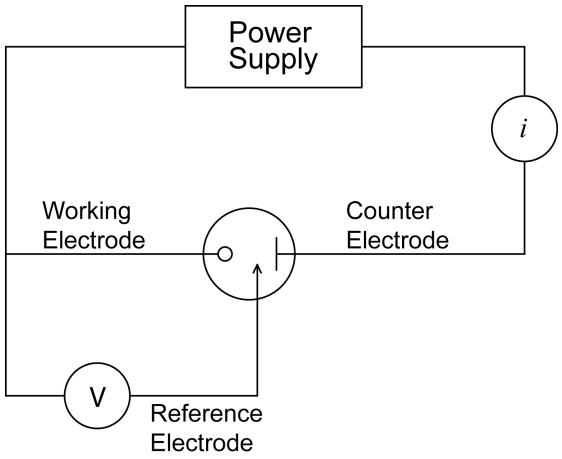

Figure 3.6: Schematic of a three-electrode half-cell.

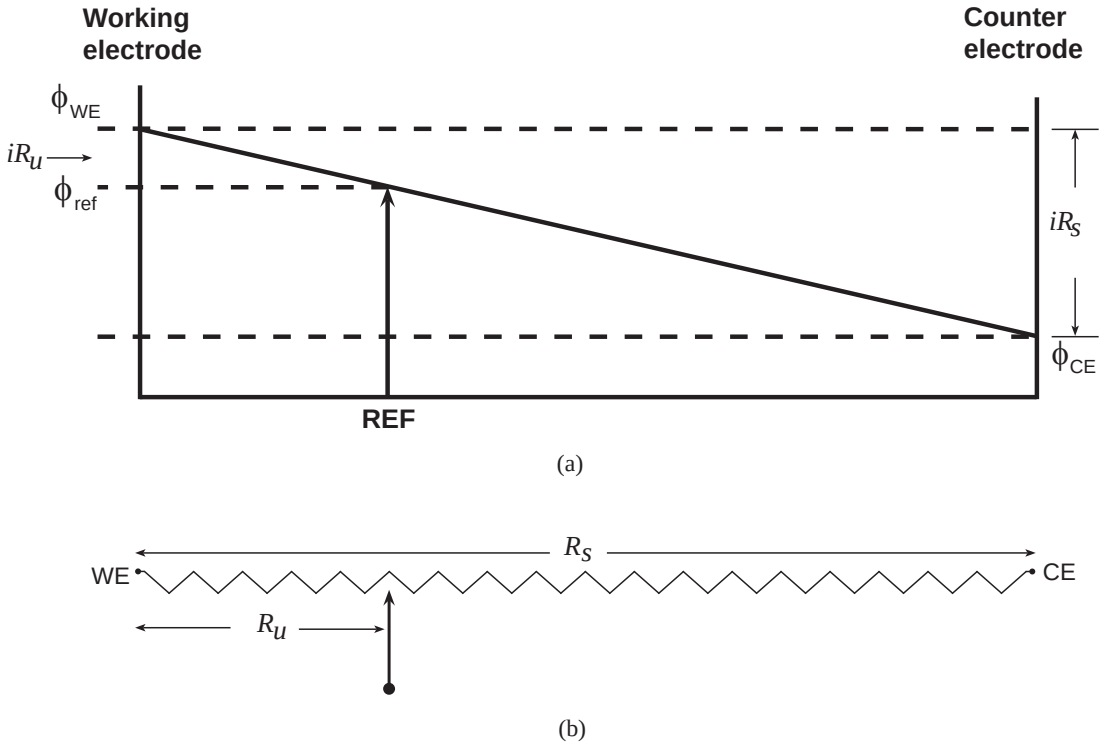

Figure 3.7: (a) Potential drop between WE and CE in solution and iR_u measured at the reference electrode. (b) Representation of the cell as a potentiometer[1].

3.3.2 Cyclic Voltammetry

Cyclic voltammetry (CV) has become a very popular technique for initial electrochemical studies of new systems and has proven very useful in obtaining information about fairly complicated electrode reactions[1]. The power of CV results from its ability to rapidly provide considerable information on the thermodynamics of a redox process, the kinetics of heterogeneous electron transfter reaction and on coupled chemical reaction or adsorption processes. In cyclic voltametry the WE potential is ramped linearly versus time to a set potential; once the potential is reached, the potential ramp is reversed.

In Figure 3.8a, λ is the switching time when the voltage is reversed on the WE. When the electrode potential reaches the vicinity of $E^{0'}$ the reduction begins and a current starts to flow. As the potential continues to grow more negative, the surface concentration of ions must drop; hence the flux to the surface (and the current) increases. As the potential moves past $E^{0'}$, the surface concentration drops nearly to zero, mass transfer of ions to the surface reaches a maximum rate, and then it declines as the depletion effect sets in. The observation is therefore a peaked current-potential curve like that depicted in 3.8b.

Once the potential scan is reversed the potential is sweeping in a positive direction, and in the electrodes vicinity there is a large concentration of the oxidizable anion. As the potential approaches, then passes $E^{0'}$, the electrochemical balance at the surface grows more and more favorable toward the neutral species[1]. Then the anion radical becomes re-oxidized and an anodic current flows. This reversal current has a shape very similar to the forward peak for essentially the same reasoning. The shape of the curve in Figure 3.8b on reversal depends on the switching

potential, E_λ, or how far beyond the cathodic peak the potential sweep is allowed to proceed before reversal of the potential.

Table 3.2: Definitions of cathode and anode electron transfer process.

Electrode	Electron transfer process
Cathode	Reduction (gain electron(s))
Anode	Oxidation (loss of electron(s))

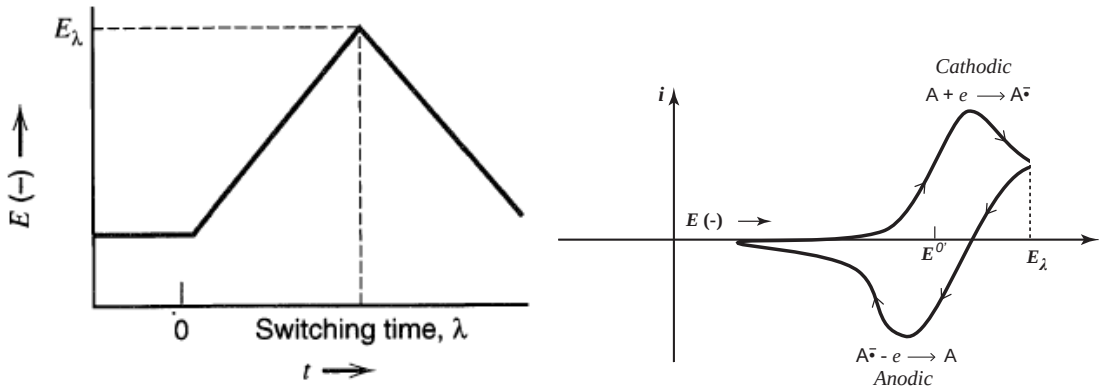

(a) (b)

Figure 3.8: (a) Cyclic potential sweep (b) Resulting cyclic voltammogram[1].

3.3.3 Chronopotentiometry

Chronopotentiometry is used to study mechanism and kinetics of chemical reactions. In this technique, the instrument operates in galvanostatic mode to control current and measure voltage. The basis of controlled current experiments is that two half-cell reactions, reduction and oxidation, must occur at the surface of the working electrode in order to support the applied current. One advantage of all

constant current techniques is that the potential drop due to solution resistance is also constant, as the ohmic drop is equal to the product of the current and the solution resistance. The ohmic drop can therefore be simply corrected by a constant potential offset. In contrast, for potentiostatic experiments (e.g., cyclic voltammetry), the current, and therefore the potential drop, varies with potential, and correction is more complicated.

3.3.4 Electrochemical Impedance Spectroscopy

Most Electrochemical Impedance Spectroscopy (EIS) experiments are performed using a potentiostat. This electronic device is used to apply both a direct current (DC) potential and a small superimposed alternating current (AC) excitation to a sample immersed in a solution. In the most common EIS experiment, AC current and AC potential are measured while the frequency of the excitation is varied over a very wide range, normally more than six decades in frequency. The cell voltage and current are then converted into a complex impedance. Unlike impedance measurements in other fields, electrochemical impedance systems also have to measure DC current and potential. The DC values are required for intelligent auto-ranging decisions made by the potentiostat.

Analysis of complex impedance versus frequency curves provide information that are not easily or accurately available from other electrochemical techniques, such as, faradaic impedance, double layer capacitance and ohmic resistance of the EC being tested. This is unique, in that, all these properties can be determined using a single EIS measurement. EIS is very useful in the evaluation of coatings, analysis of electron transfer and rates and the evaluation of battery performance.

Mass transfer limited systems have a well-defined EIS behavior that can be separated from kinetically controlled behavior[1].

For modeling EIS data using Ohm's law (equation 3.24) one can define electrical resistance as the ability of a circuit element to resist the flow of electrical current. Ohm's law defines resistances as the ratio between voltage (E) and current (I)

$$R = \frac{E}{I} \tag{3.24}$$

True circuit elements have a much more complex ohmic behavior. Therefore, the frequency dependent complex impedance is used, which is a general circuit element. EIS is based on the application of a sinusoidal voltage (or current) signal to the EC cell. The applied potential is small ($\leq 10\,\mathrm{mV}$) to avoid activation of electrochemical reactions during the measurements. The response of the cell to the sinusoidal perturbation is a sinusoidal current (or voltage), which has the same frequency as the perturbation but is normally shifted in phase. It is possible to transform the perturbation and the response using the Euler relationship (equation 3.29) of the complex impedance. The ratio between the perturbation and the response is a frequency-dependent complex number, which is, the complex impedance. The current (or voltage) response has a time harmonic which is linearly related to the applied sinusoidal signal with a phase shift dependent on the linear and nonlinear capacitance properties of the cell.

The input signal is represented as a function of the form

$$\mathrm{E_t} = \mathrm{E_0 sin}(\omega \mathrm{t}), \tag{3.25}$$

where $\mathrm{E_t}$ is the potential at time t, $\mathrm{E_0}$ is the amplitude of the signal, and ω is the radial frequency. The relationship between the radial frequency ω and the

frequency f is

$$\omega(\mathrm{rad\,s^{-1}}) = 2\pi f(\mathrm{Hz}). \tag{3.26}$$

If the system is linear the output signal $\mathrm{I_t}$ will be shifted in phase(ϕ) and will have a different amplitude $\mathrm{I_0}$, where

$$\mathrm{I(t)} = \mathrm{I_0 cos}(\omega \mathrm{t} - \phi). \tag{3.27}$$

Using Ohm's, law an expression to calculate the impedance of the system can be written as

$$\mathrm{Z} = \frac{\mathrm{E(t)}}{\mathrm{I(t)}} = \frac{\mathrm{E_0}\cos(\omega \mathrm{t})}{\mathrm{I_0}\cos(\omega \mathrm{t} - \phi)} = \mathrm{Z_0}\frac{\cos(\omega \mathrm{t})}{\cos(\omega \mathrm{t} - \phi)}. \tag{3.28}$$

Now by using Euler's relationship,

$$\exp(\jmath\omega) = \cos\phi + \jmath \sin\phi, \tag{3.29}$$

one can represent the impedance in complex form as follows:

$$\mathrm{Z} = \frac{\mathrm{E}}{\mathrm{I}} = \mathrm{Z_0}\exp(\imath\phi) = \mathrm{Z_0}\cos\phi + \imath\sin\phi. \tag{3.30}$$

3.3.4.1 Impedance Analysis

Using the approach described in section 3.3.4, it is possible to create an equivalent circuit model. This approach makes an analogy between the processes in the electrochemical cell and in electrical circuit components such as resistors and capacitors[20].

The impedance response of a passive circuit element is defined as:

$$\mathrm{Z} = \frac{\Delta \mathrm{V}}{\Delta \mathrm{I}}. \tag{3.31}$$

For a resistor, Equation 3.31 yields

$$Z_{\text{resistor}} = R, \tag{3.32}$$

for a capacitor

$$Z_{\text{capacitor}} = \frac{1}{\jmath\omega C}, \tag{3.33}$$

and for an inductor

$$Z_{\text{inductor}} = \jmath\omega L. \tag{3.34}$$

Another special impedance element often used is called a Constant-Phase Element(CPE). Compared to a parallel combination of a capacitor and resistor, the CPE is able to achieve a much better fit to most impedance data. The CPE uses only three parameters ($R_e, Q,$ and α) giving it only one more than a standard parallel RC circuit. By allowing α to take values from -1 to 1, the CPE element becomes an extremely flexible fitting element. When $\alpha = 1$, the CPE behaves as a capacitor, for $\alpha = 0$, the CPE behaves as a resistor; and for $\alpha =$ -1 the CPE behaves as an inductor[21]. The impedance of an ideally polarizable or blocking electrode, CPE is expressed as

$$Z(\omega) = R_e + \frac{1}{\jmath\omega^{\alpha} Q}. \tag{3.35}$$

For the impedance associated with a simple Faradaic reaction without diffusion, the CPE is expressed as

$$Z(\omega) = R_e + \frac{R_t}{1 + \jmath\omega^{\alpha} Q}. \tag{3.36}$$

Furthermore, DC potential control is always used with impedance measurements to control the electrochemical reactions at the surface of the electrode while the impedance measurement is preformed. The DC potential applied during an EIS

measurement on a coating is almost always the open-circuit potential. For a coated metal sample that is in excellent condition, it is difficult to obtain a stable value of the open-circuit potential. The non-electroactive nature of the coatings causes the sample to behave like a capacitor, for which an open-circuit potential is undefined[20].

3.3.4.2 Capacitor Model Used to Determine Film Thickness

After using EIS equivalent circuit models to best match EIS data, one obtains capacitances associated with the model circuit elements. Using these capacitance values one can employ the parallel plate capacitor model for thin film thickness approximations. The capacitance of two flat parallel plates of an area A, and separation d is given by the expression:

$$C = \frac{\varepsilon A}{d} = \frac{k\varepsilon_0 A}{d}, \tag{3.37}$$

where ε_0 is the permittivity of space equal to 8.854×10^{-12} F m^{-1} and k is the relative permittivity of the dielectric material between the plates. One can easily solve for the thickness (d) of the capacitor if all other variables are known.

3.3.4.3 Electric double layer

The electric double layer (DL) is the structure of charge accumulation and charge separation that always occurs at the interface when an electrode is immersed into an electrolyte solution. The excess charge on the electrode surface is compensated by an accumulation of excess ions of the opposite charge in the solution. The amount of charge is a function of the electrode potential. This structure behaves essentially as a capacitor. There are several theoretical models that describe the

structure of the double layer. The three most commonly used are the Helmholtz model, the Gouy-Chapman model, and the Gouy-Chapman-Stern model.

3.3.4.4 Nyquist Plots

According to Equation 3.30 the complex impedance is composed of real and imaginary parts. In a Nyquist plot the real part of Equation 3.30 is plotted on the X-axis and the imaginary part on the Y-axis of the graph (Figure 3.9a). Each point on the plot corresponds to a frequency. To model data from EIS experiments, one can use simple equivalent circuit components such as resistors, capacitors, inductors and other, more specialized elements if needed. The Nyquist plot in Figure 3.9a, for example, can be modeled using a single time-constant, parallel RC circuit, schematically shown in Figure 3.9b.

3.3.4.5 Bode Plots

Another presentation method of the complex impedance is the Bode plot. In a Bode plot, a log scale of frequency is on the X-axis and the log of the absolute value of the impedance($\log |Z|$) on the left Y-axis, and the phase shift ϕ is on the right Y-axis. A Bode plot for the parallel RC circuit in 3.9b is pictured in 3.10. The Bode plot has an advantage over a Nyquist plot in that, because each data point in the plot can be directly related to a frequency.

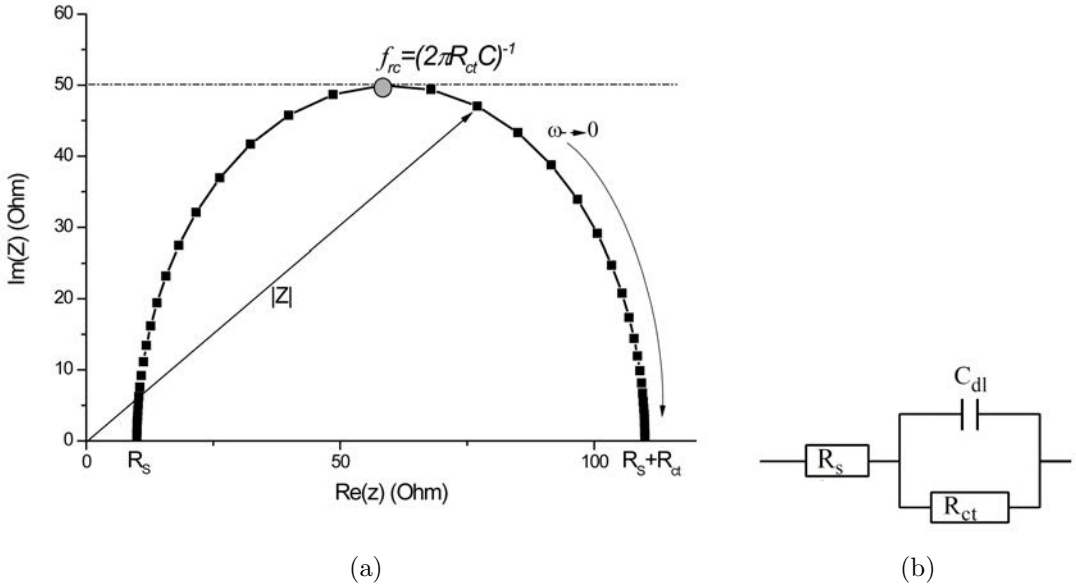

(a) (b)

Figure 3.9: (a) Nyquist plot of EIS data where impedance falls as frequency rises. The equivalent circuit used to generate the plot is depicted in (b). $R_s = 10\,\Omega$, $R_{ct} = 100\,\Omega$, $C_{dl} = 20\,\mu F$.

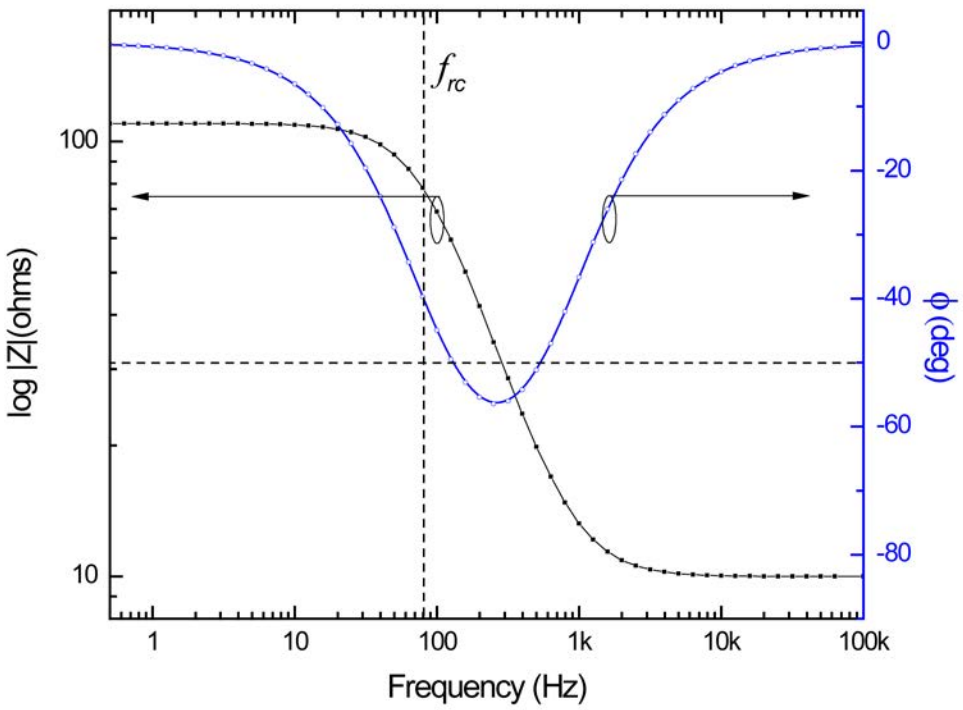

Figure 3.10: Bode plot of a single time-constant parallel RC circuit in Figure 3.9b. $R_s = 10\,\Omega$, $R_{ct} = 100\,\Omega$, $C_{dl} = 20\,\mu F$.

Chapter 4

Experimental

4.1 Setup

The experimental setup brings together in-situ ellipsometry techniques and electrochemistry. A J.A. Woollam Co. M-2000U spectroscopic ellipsometer with a spectral range of 250 nm to 750 nm was used along with a Gamry Potentiostat, Galvanostat, Zero Resistance Ampmeter (Series G 750). The Gamry Series G 750 has an output current of ±750 mA and a compliance voltage of 12 V. With current ranges of ±7.5 nA to ±750 mA and a current resolution as low as 2.5 fA but is dependent on the current output, becoming less accurate as current output becomes higher.

The ellipsometer is mounted on a horizontal stage goniometer (Figure 4.2). A liquid cell made of glass is placed at the center of the goniometer. The liquid cell (Figure 4.1) has windows at a fixed angle of incidence (AOI) of 65°. The sample is lowered into the liquid cell from above and attached to a manipulation stage to allow for optical alignment of the sample with the ellipsometer beam path.

During each experiment the following steps are taken:

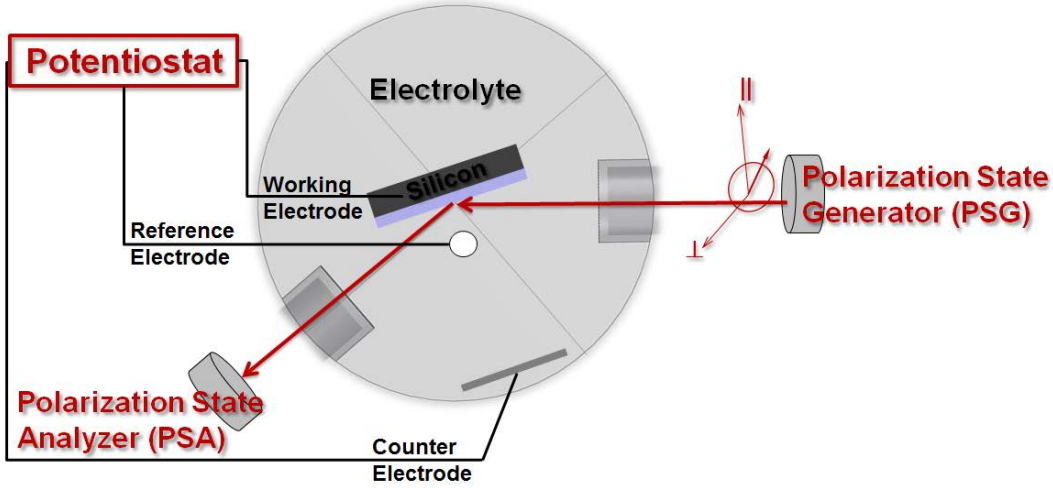

Figure 4.1: Schematic representation of the potentiostat/galvanostat/EIS hooked up to the Liquid cell. The working electrode is the sample under investigation and the counter electrode is the 99.9% titanium plate. The red arrow going through the cell from the polariztion state generator represents the ellipsometer beam path reflecting of the sample surface at a AOI of 65° the to the polarization state analyzer.

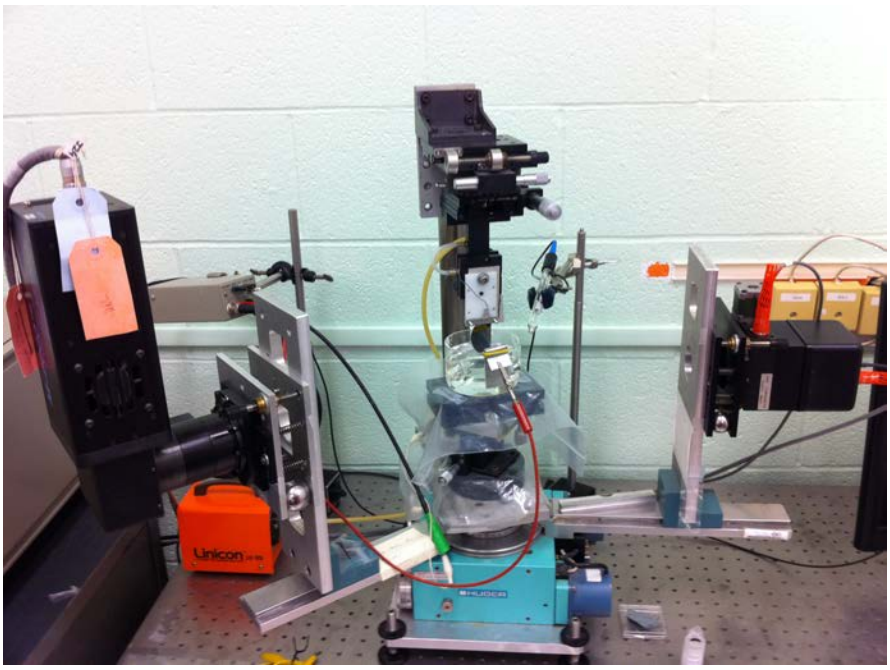

Figure 4.2: Picture of M-2000, vertically mounted to a goniometer. The EC cell is set on the platform located in middle of the setup were the sample can be lowered into the EC cell and optically aligned.

1. Ellipsometer is calibrated using a Si/SiO_2 calibration wafer
2. SE measurement is taken on sample with no cell present
3. Cell is introduced into beam path and SE measurement is taken on sample
4. Liquid is added to cell and SE measurement is taken on sample
5. In-situ SE measurement is started
6. Potentiostat or galvanostat experiment is started and logged into SE software
7. After experiment is done, sample is measured outside of cell (ex-situ)

4.1.1 Anodic Oxidation of Silicon

We first investigate the anodic oxidation of Si, which is an optically well characterized material. Ellipsometric measurements are performed in-situ through the liquid cell described in Figure 4.1. Using the process outlined in Tiwald et al.[47] silicon dioxide (SiO_2) is anodically grown. A 2" diameter n-type Si wafer was cleaved in half and used as the WE in the half-cell, a piece of 99.9% titanium (Ti) metal was used as the CE and a Ag/AgCl electrode from CH Instruments, Inc. was used as the reference electrode. The cell electrolyte solution was a mixture of ethylene glycol, water and potassium nitrate. The proposed anodic reaction is[47]

$$\mathrm{Si} + 2\,\mathrm{H_2O} \longrightarrow \mathrm{SiO_2} + 4\,\mathrm{H^+} + 4\,\mathrm{e^-}. \tag{4.1}$$

Looking at Equation 4.1, the production of SiO_2 relies on the presence of water. Therefore, the growth rate will depend on the fraction of water in the solution.

The chosen electrolyte solution for this experiment was 90% ethylene glycol, 10% deionized water and 0.05 M potassium nitrate.

Each sample is cyclicly oxidized using chronopoteniometry. The first 20 cycles were applied for 2 min and second 20 cycles for 5 min, each. The current desitity was set to $30\,\mu A\,cm^{-2}$ for each chronopoteniometry scan. After applying current for 2 min an EIS measurement was taken. Then the next chronopoteniometry scan was started. This process was repeated for 20 cycles at 2 min and then 20 cycles at 5 min.

4.1.2 Intercalation of Lithium into Silicon

Si anodes were investigated using *n*-type crystalline Si and then thin films of amorphous Si (*a*-Si). The same basic procedure outlined in the beginning of this chapter was used. The *n*-Si wafers were cleaned thoroughly in acetone in an ultrasonic bath, rinsed with 99.9% ethanol and dried with nitrogen before use. The *a*-Si was grown by evaporation under ultra-high vacuum onto *n*-type wafers with a previously sputtered gold film of 120 nm. The samples are used as the WE in the liquid cell. The same CE and reference electrode was used as in the anodically grown SiO_2 case. The electrolyte used was a 0.1 M solution of lithium perchlorate ($LiClO_4$) in dimethylformamide (DMF).

DMF is an organic compound with the formula $(CH_3)_2NCOH$. It is a colorless liquid and a polar (hydrophilic) aprotic solvent. DMF was selected as the solvent for the lithium perchlorate since it has no free oxygen for the Li-ion to react with. Lithium perchlorate is also extensively used as an electrolyte in lithium batteries, as it does not undergo oxidation on the anode.

Chapter 5

Results and Discussion

5.1 Anodically Grown SiO_2

5.1.1 In-Situ Spectroscopic Ellipsometry

For the growth of anodically grown SiO_2, optical constants of the electrolyte were measured by a minimum beam deviation technique using a standard J.A. Woollam Co., Inc. variable angle spectroscopic ellipsometry (VASE) instrument[24]. This allowed for the measurement at room temperature. The experimental data is modeled using a two layer stack (see Figure 5.1) with crystalline silicon as the substrate and a Sellmeier layer on the top. The top layers Sellmeier function uses the parameters of $\varepsilon(\infty) = 1$, $A = 0.994$, $B = 0.0977$ and $E = 0.0075$ in the spectral range of 300 nm to 1400 nm (see Figure 5.2). The crystalline silicon optical constants from the CompleteEASE software were used for all models. The Sellmeier layer calculated optical constants were then used in the final model used for best-matching the in-situ dynamic data taken while the SiO_2 was grown anodically. All ex-situ ellipsometry measurements before and after growth are taken using a J.A. Woollam Co. M-2000 *VI* in the spectral region of 360 nm to 1600 nm

to confirm the film thickness.

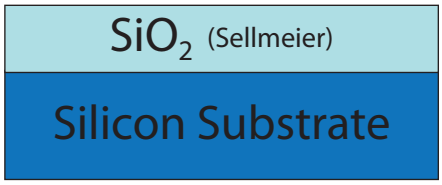

Figure 5.1: Simple two layer model used for modeling the anodically grown SiO_2.

CompleteEASE software from the J.A. Woollam Co., Inc. was used for all ellipsometric data analysis. Using the tabulated optical constants from CompleteEASE for native SiO_2 (Figure 5.3), the starting best-match calculated thickness of the sample SiO_2 film is 3.72 nm and Figure 5.4 shows the best-match model for Ψ and Δ using the optical constants for native oxide on Silicon[34]. The simple two-layer model used for modeling the in-situ data is depicted in Figure 5.1. The in-situ dynamic Sellmeier function uses the parameters of $\varepsilon(\infty) = 0.417$, $A = 1.664$, $B = 0.1014$ and $E = -0.0421$. Figure 5.5 shows the in-situ best-match model thickness change allowing only the thickness to be varied during the best-match model calculation. The starting thickness during the in-situ measurement is 3.68 nm until the first electrochemical cycle is started around 7 min. During the first charge cycle starting at 7 min the largest change of 0.8 nm is seen. One can also derive from Figure 5.5 that the in-situ ellipsometry is very sensitive to the electric double layer that is formed while the current is being supplied across the sample. When the applied current is stopped to take an EIS measurement the thickness drops by approximately 0.3 nm during each SiO_2 growth cycle. The final in-situ Sellmeier model thickness is (10.5±0.085) nm.

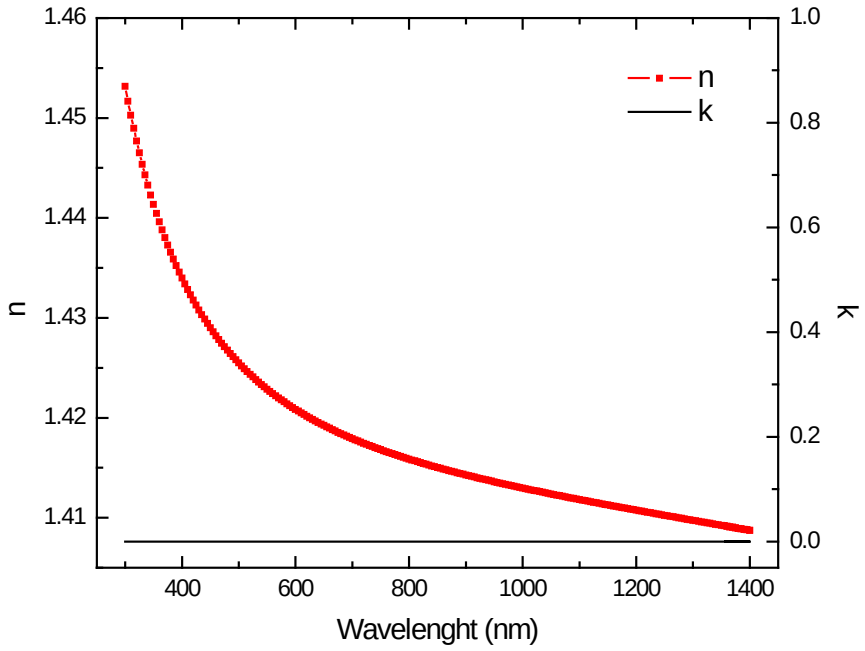

Figure 5.2: Model calculated optical constants of electrolyte solution used for anodically grown SiO_2 of 90% ethylene glycol, 10% deionized water and 0.05M potassium nitrate at 25 °C. Measured using minimum beam deviation technique[24]. Modeled using a Sellmeier function with the parameters of $\varepsilon(\infty) = 1$, $A = 0.994$, $B = 0.0977$ and $E = 0.0075$ in the spectral range of 300 nm to 1400 nm

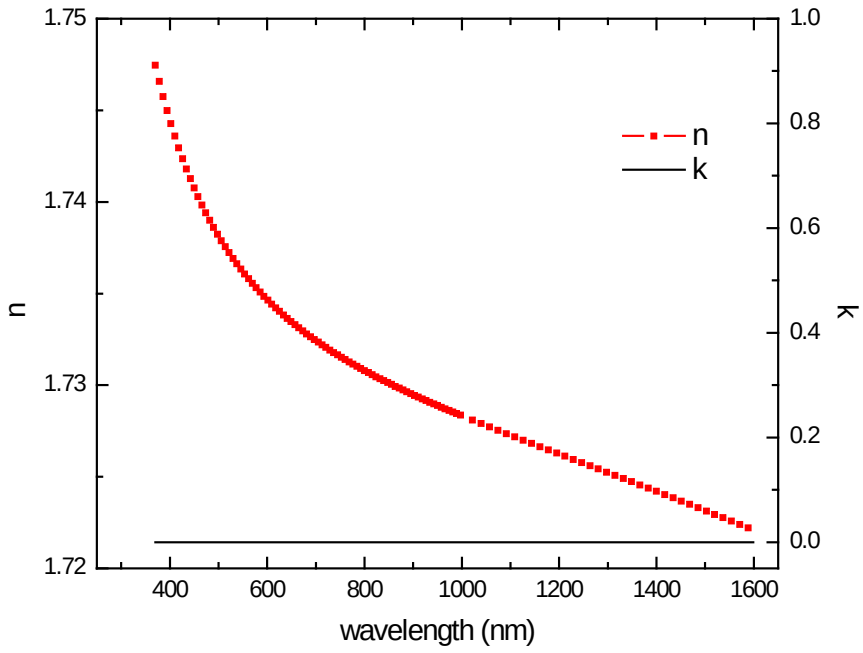

Figure 5.3: Optical constants n and k for native SiO_2.

The model calculations in Figures 5.6 and 5.7 show the best-match models to Ψ and Δ dynamic data. Figure 5.7 highlights that Δ is very sensitive to thickness variations, while Ψ on the other hand seems to not fit as well but is only changing by a small degree showing that there is only a very small change in the amplitude ratio of the p and s polarized light after reflection from the sample.

Since the calculated optical constants of the Sellmeier model were very close to that of thermal SiO_2 a comparison of best-match model thickness calculated for before oxidation (ex-situ), during (in-situ) oxidation, and after (ex-situ) is given in Table 5.1. This table shows that the Sellmeier model calculations match both the before and after ex-situ calculated thicknesses using native oxide optical constants for before oxidation and the thermal oxide optical constants for after oxidation.

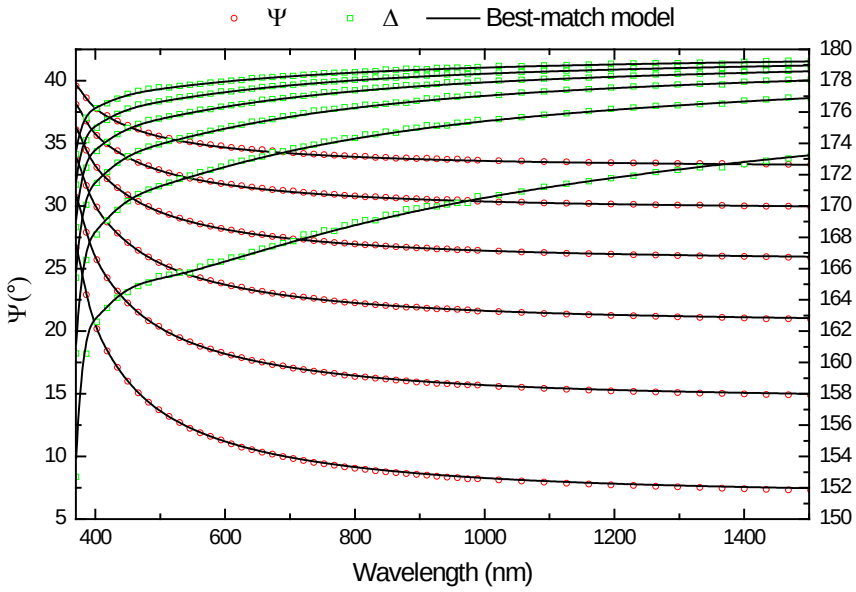

Figure 5.4: Experimental (solid lines) and Best-matched model (black dashed lines) for Ψ and Δ versus wavelength using native oxide optical constants, before anodic oxide growth. Measured at multiple angles of incidence (Φ_a = 45°, 50°, 55°, 65°, 70°, 75°).

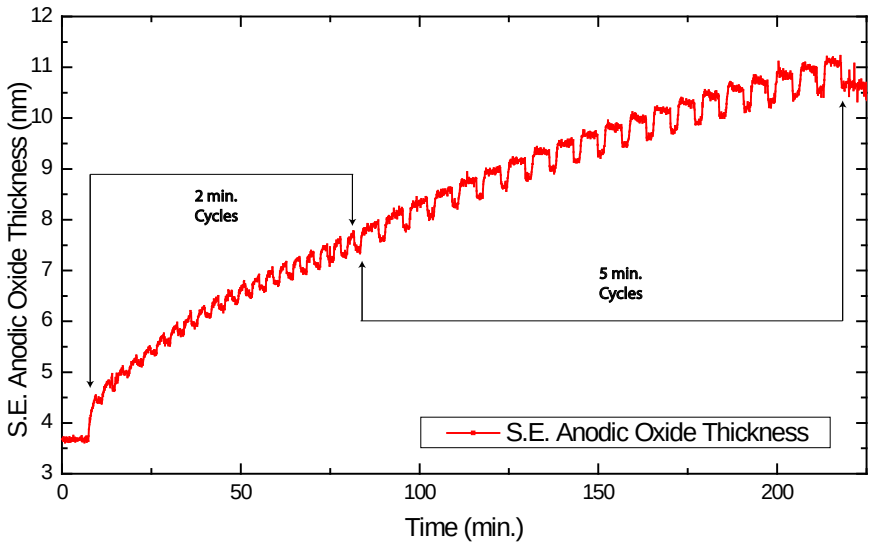

Figure 5.5: Plot of best-match model dynamic thickness using the Sellmeier function. Showing the increase over time for anodically grown SiO_2.

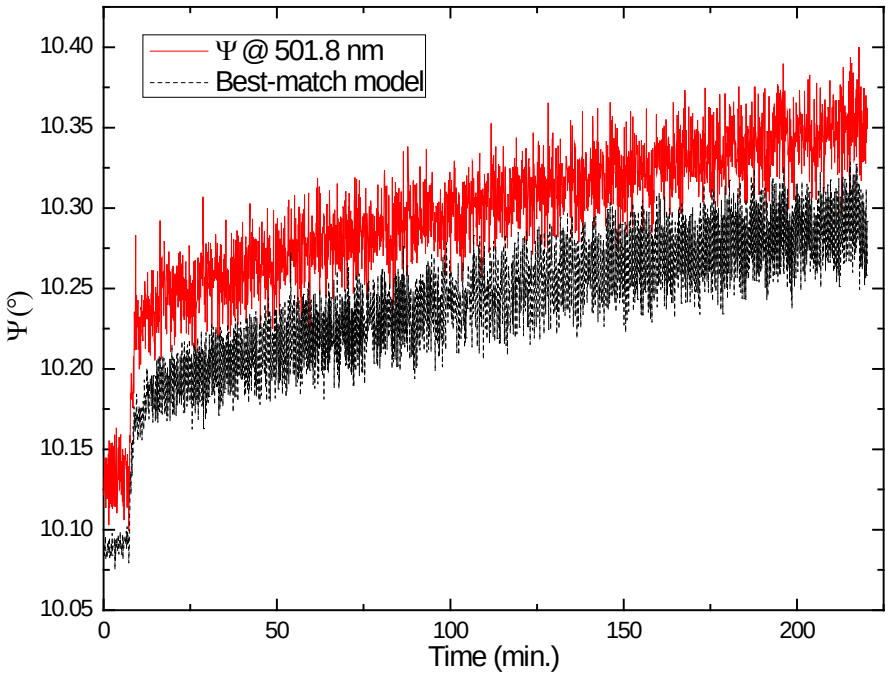

Figure 5.6: Best-matched model(dotted line) to dynamic data for Psi.

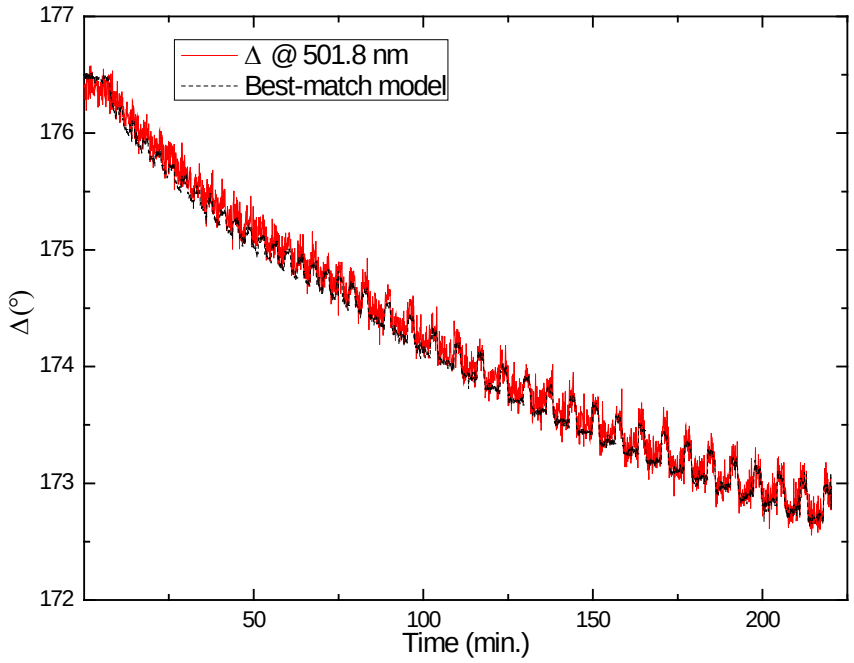

Figure 5.7: Best-matched model(dotted line) to dynamic data for Delta.

Also shown in Figure 5.8 is the optical constants n and k of both thermally grown SiO_2 and the best-match model calculated from the Sellmeier function.

Table 5.1: Comparison of Thermal, Sellmeier, and native SiO_2 SE Model Calculated Thicknesses

	Before	in-situ	After	Units
Thermal SiO_2	4.38	4.18-11.85	10.15	nm
Sellmeier Model	4.36	3.68-10.64	10.09	nm
Native SiO_2	3.71	.72-2.13	8.58	nm

All numerical data possess less than 1% error.

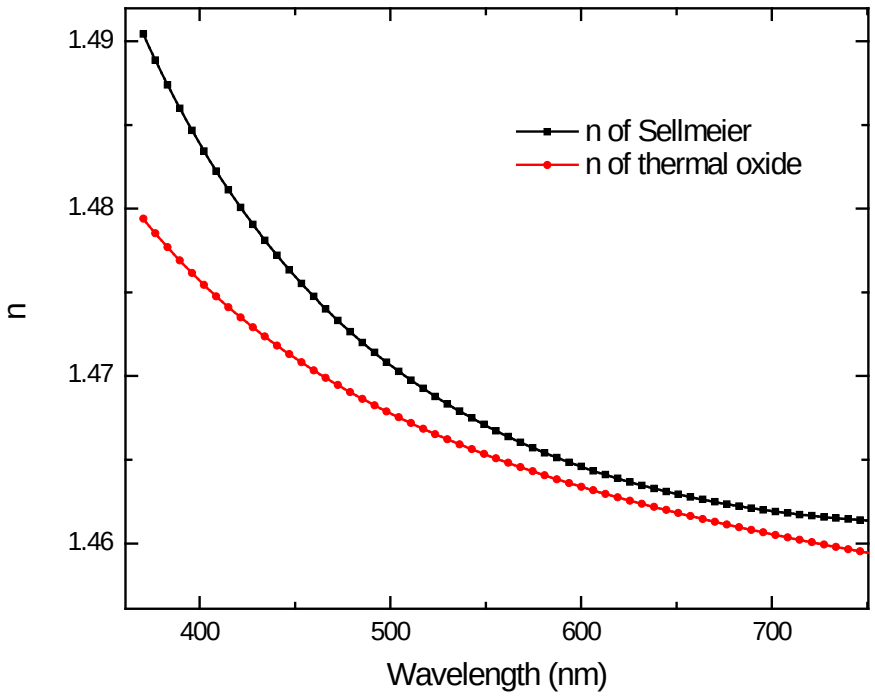

Figure 5.8: Optical constants n and k calculated from best-match Sellmeier model for anodically grown SiO_2, compared to tabulated thermally grown SiO_2 [34].

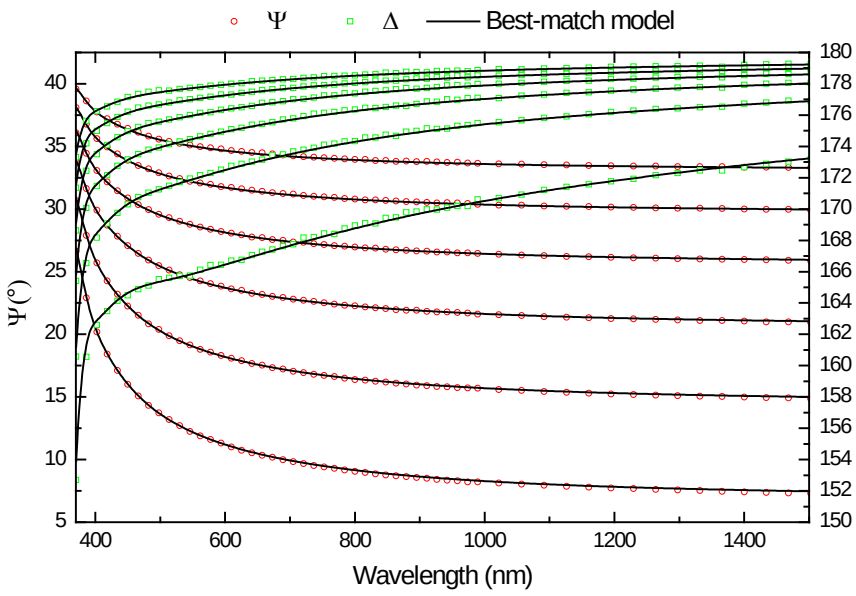

Figure 5.9: Best-matched model(dotted line) to anodically grown SiO_2 measured ex-situ.

5.1.2 Electroanalysis of SiO_2

Samples were cycled as described in Section 4.1.1. Figure 5.10 shows the voltage versus time plots for a selected number of cycles for clarity. The monitored potential increases continuously and plateaus during each cycle. During the 16th 5 min cycle the voltage reaches the maximum of 12 V, which is the limiting potential of the potentiostat. Each EIS measurement was taken in the spectral range of 200 mHz to 300 kHz. Using the RC equivalent circuit shown in Figure 5.11, and using three parallel RC circuits C_{cell} and R_{cell}, C_{dl} and R_{dl}, C_{ox} and R_{ox} one can represent the EC cell, the electronic double layer and anodically grown SiO_2, respectively. The equivalent circuit model was then fit to the EIS using a LevenbergMarquardt algorithm using Gamry Echem Analyst.

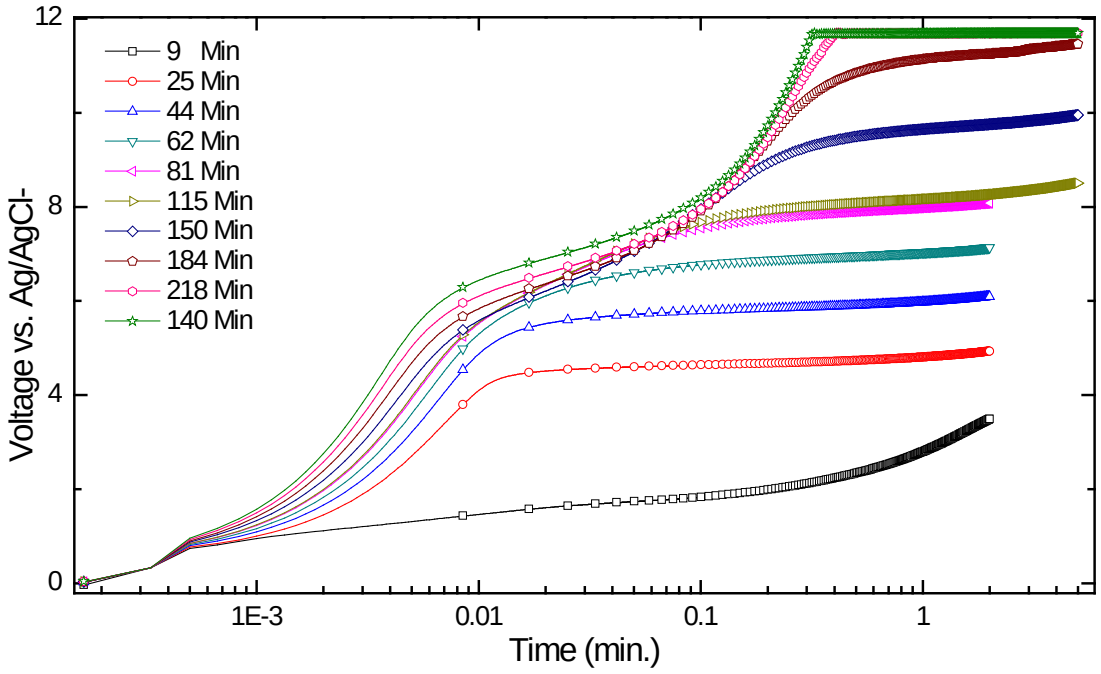

Figure 5.10: Voltage versus time plots for the anodically grown SiO_2. To apply the constant current of $30\,\mu A\,cm^{-2}$ the voltage between the working and counter electrodes is allowed to vary (chronopotentiometry). The above plot shows the constant increase in voltage needed in each subsequent cycle. Only growth cycles 1,5,10,15 and 20 in the 2 and 5 min. cycles are shown for clarity. The maximum output voltage allowed by the Gamry galvenostat is 12 V, this voltage is reached starting in the 15th 5 min. cycle. After each chronopotentiometry cycle the an EIS spectrum is measured.

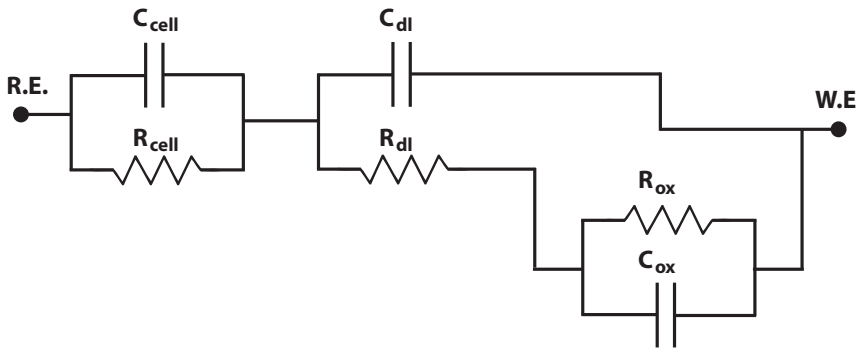

Figure 5.11: Equivalent circuit model used for modeling SiO_2 EIS data.

Table 5.2 shows the best-match model calculation parameters for the measured EIS data, and the calculated thickness for the anodically grown SiO_2 layer using the parallel plate capacitor model from equation 3.37. Figure 5.12 shows the best-match model line shape fits and experimental EIS data. When using Equation 3.37 the relative permittivity k is set to the known value of SiO_2 at 3.9[30]. As the SiO_2 thickness increases as confirmed by in-situ SE higher resistance and lower capacitance is expected and is confirmed in table 5.2. The calculated oxide thickness using EIS modeling shows good agreement with the SE measurements, with only an average offset of 1.76 nm between the calculated SE and capacitance thicknesses.

Figure 5.13 shows the individual parallel RC circuit contributions to the model for before and after SiO_2 growth. This plot highlights the shifting cut-off frequency of each of the parallel RC circuits used in the EIS model. By adding the line shapes of each individual resistance or phase (square, circle or triangle) one arrives at the line shape that matches the solid (start or finish) line. Using the equation for the cut-off frequency ($f_c = \frac{1}{2\pi RC}$) of a parallel RC circut each time with its

Table 5.2: Best-match model electrical component values of the equivalent circuit from Figure 5.11 for the measured impedance data during SiO_2 growth . And calculated thickness using C_{ox} in Equation 3.37 to calculate the thickness of anodically grown SiO_2 and SE thickness for comparison.

Time	C_{dl}	R_{dl}	C_{ox}	R_{ox}	C_{cell}	R_{cell}	Thickness	SE Thickness
min	nF	Ω	µF	kΩ	nF	kΩ	nm	nm
0.0	0.51	395.10	22.70	35.80	6.52	349.30	2.99	3.65
9.6	0.60	389.80	24.32	118.90	6.40	197.60	2.79	4.52
24.0	0.73	383.80	18.84	361.60	6.15	22.40	3.60	5.49
43.5	0.88	380.80	15.26	355.20	6.15	22.19	4.44	6.46
82.0	1.05	375.70	11.82	577.80	6.10	13.20	5.73	7.58
116.2	1.16	373.70	9.87	733.80	6.11	8.18	6.87	8.75
150.0	1.37	371.20	8.72	888.00	6.11	8.27	7.77	9.69
218.0	1.36	383.30	7.16	1371.00	6.12	5.96	9.46	11.07
228.00	1.46	373.20	7.74	1290.00	6.07	6.21	8.76	10.56

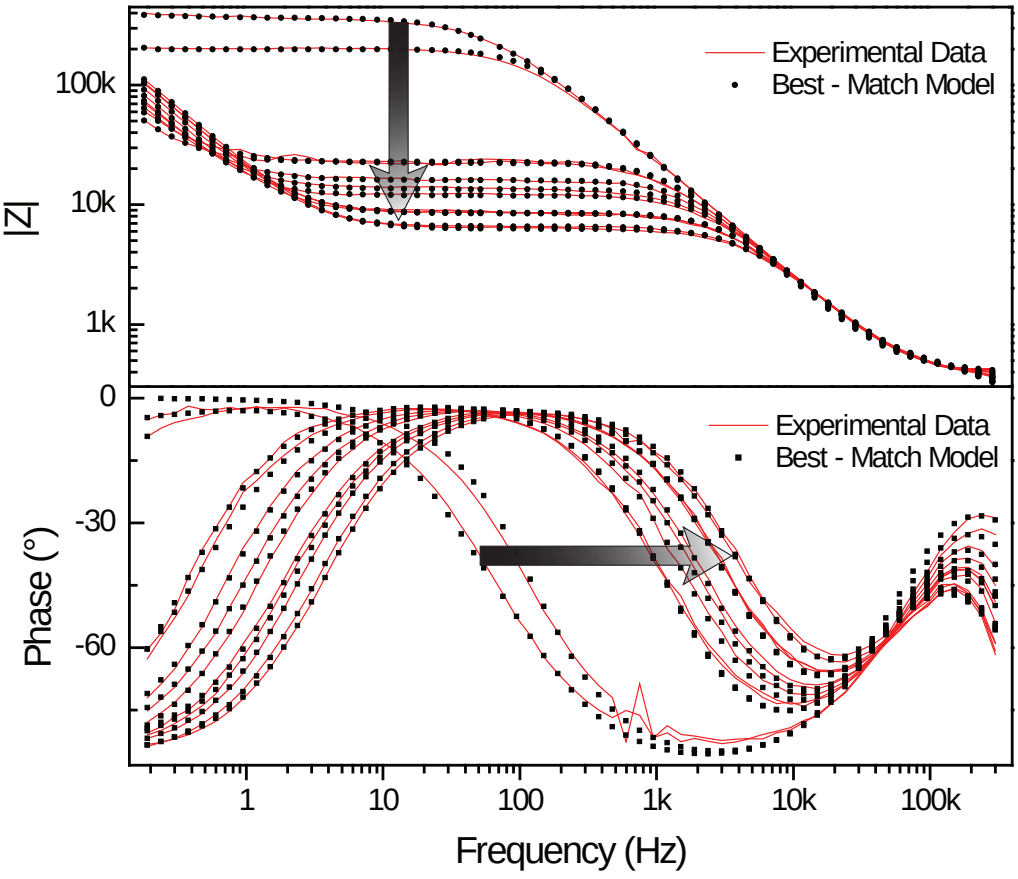

Figure 5.12: Bode plots of EIS measurements and best-match model taken after each growth cycle using a AC signal of 10 mV rms while at 0 V DC cell potential. Arrows point from first to last cycle showing the shift in the complex impedance magnitude (top) and phase (bottom).

corresponding cut-off frequency is listed in Table 5.3.

Table 5.3: Calculated cut-off frequencies of each Parrallel RC Circuit used in the equivalent circuit models for EIS measurement data of SiO_2.

Poles of Parallel RC Circuits			
Time min	Double layer kHz	SiO_2 Hz	EC Cell kHz
0	789.63	195.94	69.96
9.6	676.78	55.07	125.93
24	564.71	23.37	1156.64
43.5	473.14	29.38	1166.45
82	405.59	23.32	1977.92
116.2	368.92	21.99	3188.60
150	314.27	20.57	3149.27
218	305.24	16.22	4369.19
228	291.84	15.95	4229.85

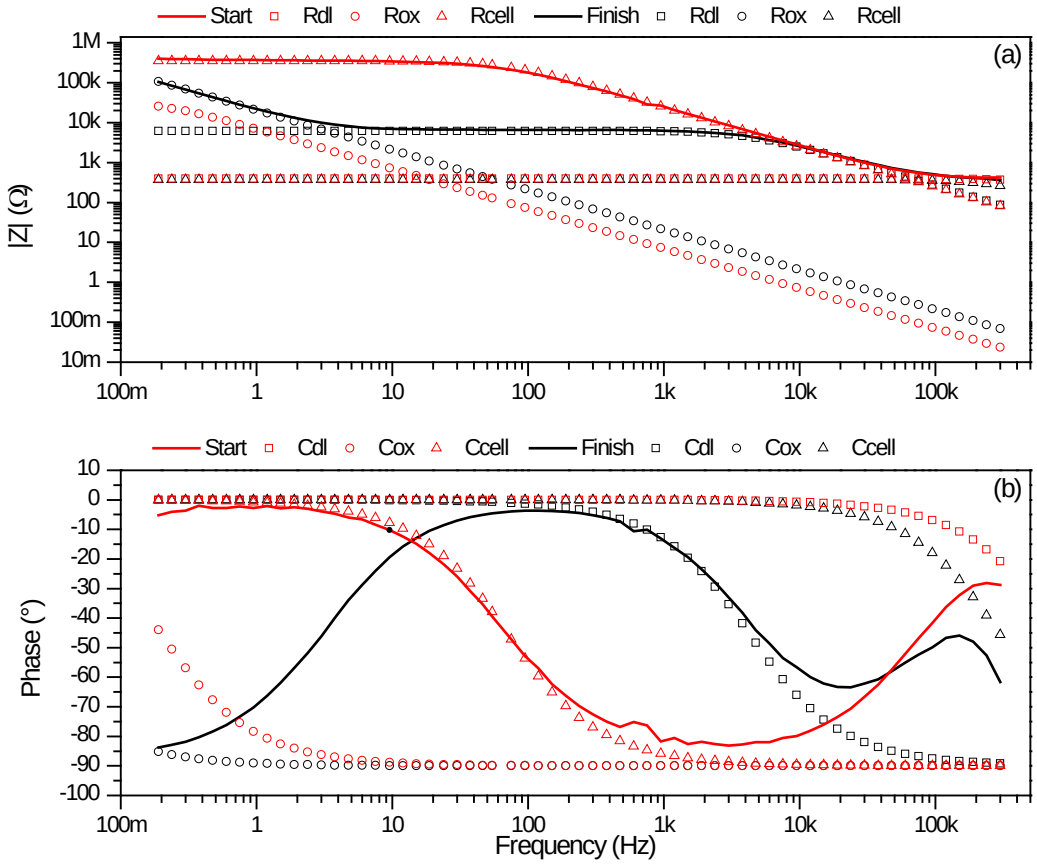

Figure 5.13: Bode plots before and after (Start and Finish) anodic SiO_2 growth with corresponding individual RC circuit elements C_{dl}, R_{dl}, C_{ox}, R_{ox}, C_{cell} and R_{cell}. This plot highlights the shifting cut-off frequency of each of the parallel RC circuits used in the EIS model. By adding the line shapes of each individual resistance or phase(square, circle or triangle) one arrives at the line shape that matches the solid (start or finish) line.

5.2 Lithium intercalation into Silicon

5.2.1 Crystalline Silicon

The crystalline Si sample was cycled through a CV measurement for 11 cycles from $-2\,\mathrm{V}$ to $0.03\,\mathrm{V}$ (Figure 5.14). During the CV simultaneously in-situ ellipsometry measurements were taken at a 65° AOI. All ellipsometric data was again analyzed using a Sellmeier model described previously using CompleteEASE software. Figure 5.1 shows the layer structure used to fit the in-situ ellipsometry data, parameters that are calculated over the time evolution are: layer thickness and the amplitude of the Sellmeier layer. The Sellmeier function parameters used are $\varepsilon(\infty) = 0.378$, $B = 0.085$ and $E = 0.010$. Ψ and Δ dynamic measurements with their best-match model calculations for the wavelength of 501.8 nm are presented in Figures 5.15 and 5.16 respectively.

Figure 5.17 shows the best-match calculated thickness and index of refraction vs. time for the Sellmeier layer. Figures 5.15 and 5.16 show the best-match model fit to Ψ and Δ, respectively. The model matches well in all intercalation/de-intercalation cycles except for the first. The final best-match model thickness is 96.72 nm, from a starting point of 0.66 nm. Although this has not been quantified at present it is indicative for either swelling or plating of the crystalline Si.

During the first cycle parameter A is very large, above 9, but quickly lowers to a reasonable value of 1.69 as does the refractive index n starting at 3.12 but going quickly down to 1.44 (Figure 5.17). Both n and A stay constant after the first half cycle as the thickness continues to increase during each CV cycle.

In Figure 5.18 current and Δ are plotted versus time, one can see that Δ

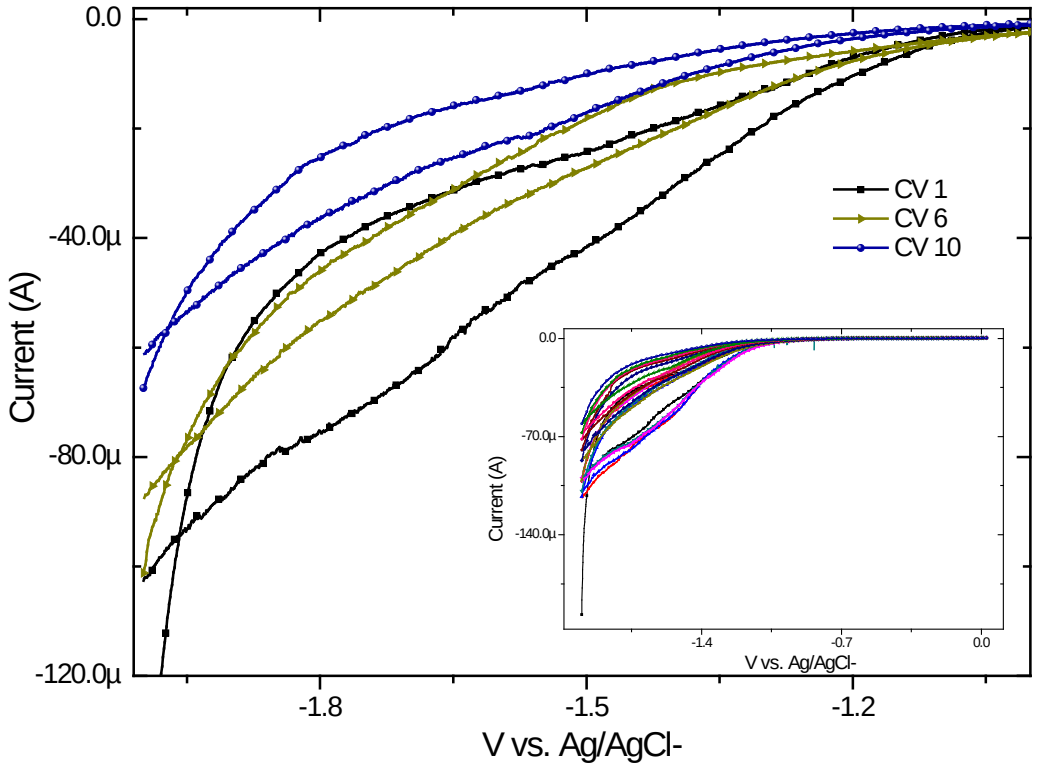

Figure 5.14: CV measurement on crystalline Si. The x-axis of the main graph is cut off at 1.3 V for clarity showing CV cycles 1, 5 and ten. The full graph is shown in the inset at the bottom right hand corner.

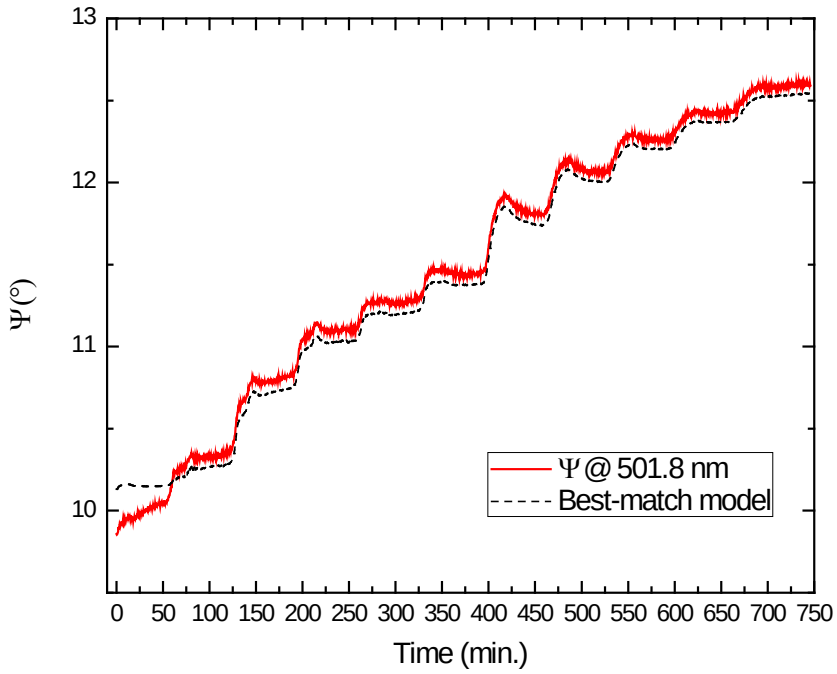

Figure 5.15: Measured Dynamic Ψ and best-match model data at the wavelength of 501.8 nm for Li intercalation into crystalline Si. Dashed lines correspond to the best-match model calculated data.

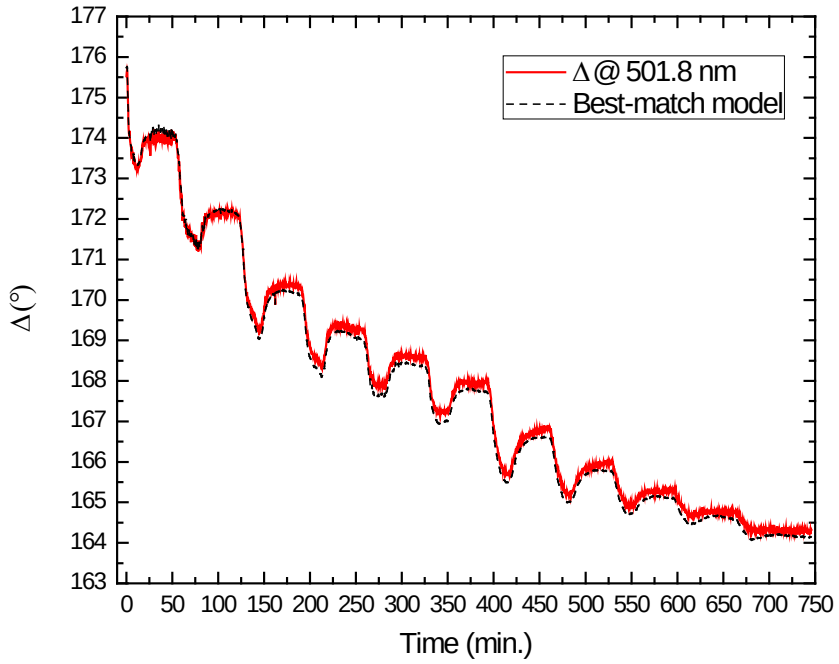

Figure 5.16: Measured Dynamic Δ and best-match model data at the wavelength of 501.8 nm for Li intercalation into crystalline Si. Dashed lines correspond to the best-match model calculated data.

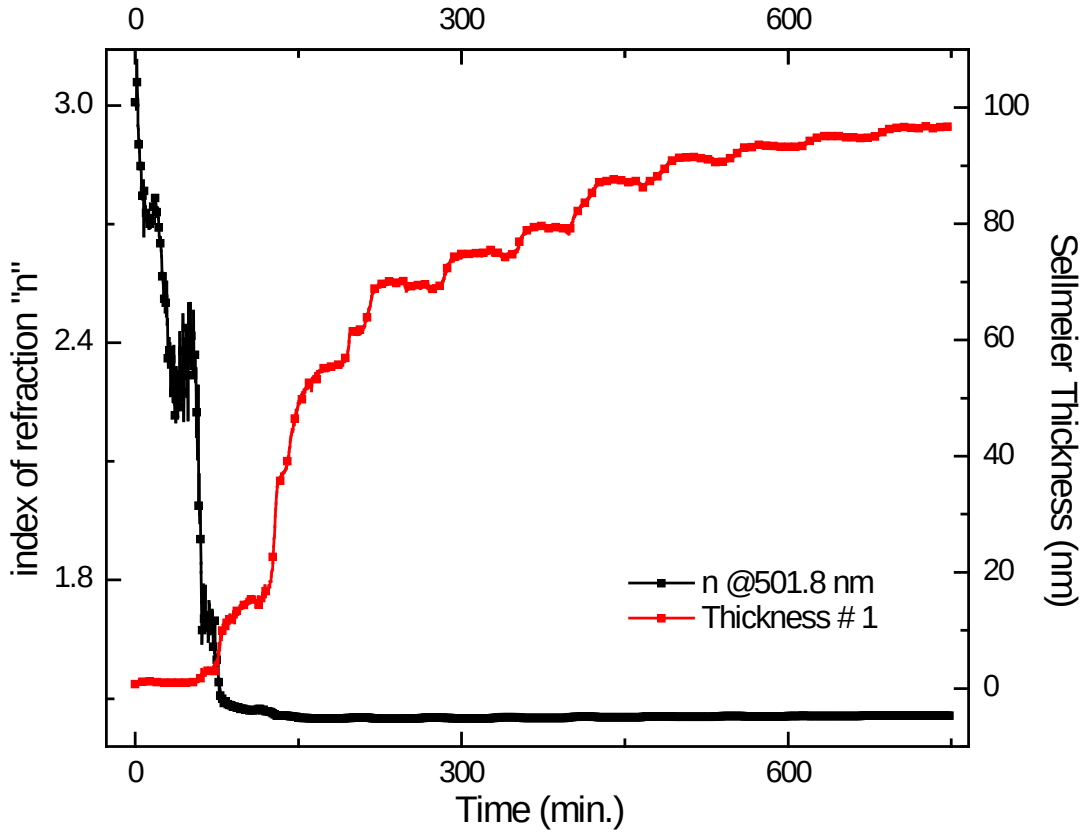

Figure 5.17: Dynamic refractive index (n) and the calculated thickness of the Sellmeier function at the wavelength of 501.8 nm for lithium intercalation into crystalline Si.

(phase information from Δ is very sensitive to film thickness) follows the current. Although Δ follows the current it is not totally reversed to its starting position. This constant drift has multiple explanations, and is likely a combination of them. First, the voltage polarity is never reversed to the positive direction long enough to force the lithium to be de-intercalated. Second, irreversible changes to the crystalline Si are occurring that has been shown in multiple sources[3,4,38,39]. If the sample is being plated with Li, the higher potentials would need to be applied strip the Li off of the Si, which are not reached apparently. One can also see in Figure 5.18 that the maximum current achieved is lower in each subsequent CV, indicating Li is being plated on the sample, and its capacity for more Li lowers in each subsequent CV cycle. The consistent increase in calculated thickness also points to plating of the sample.

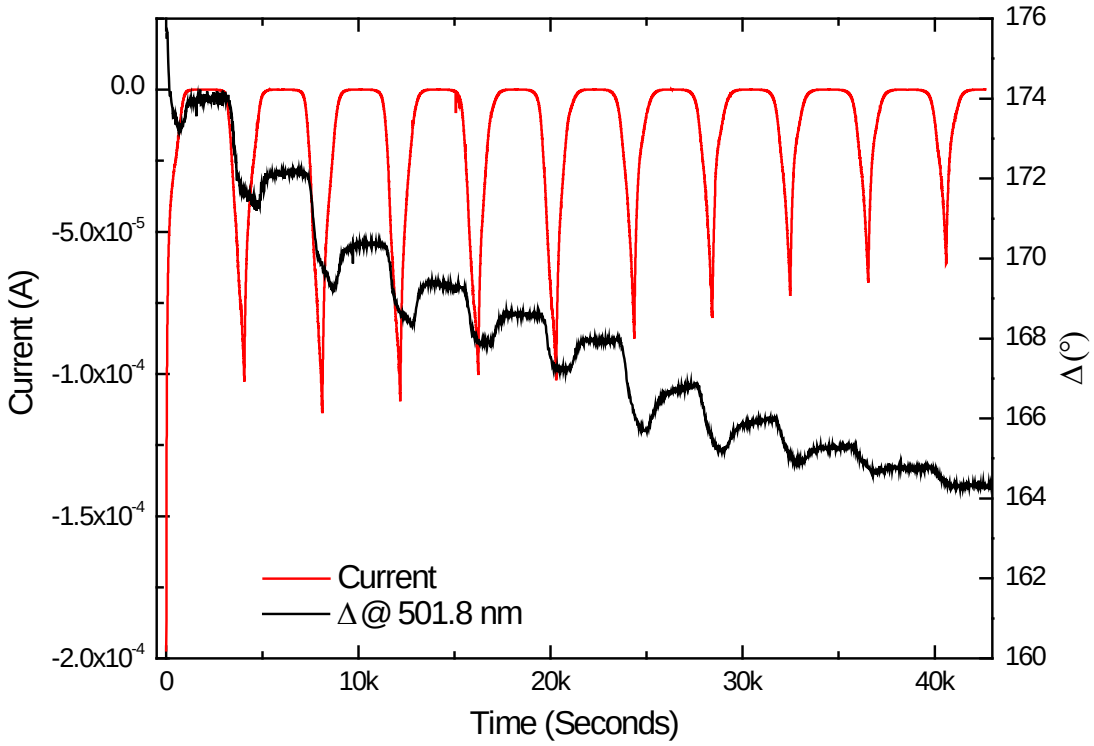

Figure 5.18: Current applied and dynamic Δ data at the wavelength of 501.8 nm versus time.

5.2.2 Amorphous Silicon

The *a*-Si sample is charged at the rate of 150 µA cm^{-2} using chronopotentiometry, a EIS spectrum is taken and then the *a*-Si sample is discharged by measuring the open circuit potential. Each charge cycle was approximately 860 s (Figure 5.19). After charging an EIS measurement is taken in the spectral range of 200 mHz to 100 kHz (figure 5.20). Next the open circuit potential is measured for 600 s or until the stability of the signal has reached ±1 mV(Figure 5.21).

Compared to the crystalline Si, the *a*-Si shows much more drastic changes in Ψ and Δ (Figures 5.22 and 5.23). But shows less cyclability, with the change in Ψ and Δ flat lining after only 5 cycles. On the fifth cycle the films had started to peel off the substrate so the measurements were halted. Bode and Nyquist plots of the EIS measurements are presented in Figures 5.20 and 5.24, respectively. They show a increasing impedance, but no significant change in phase.

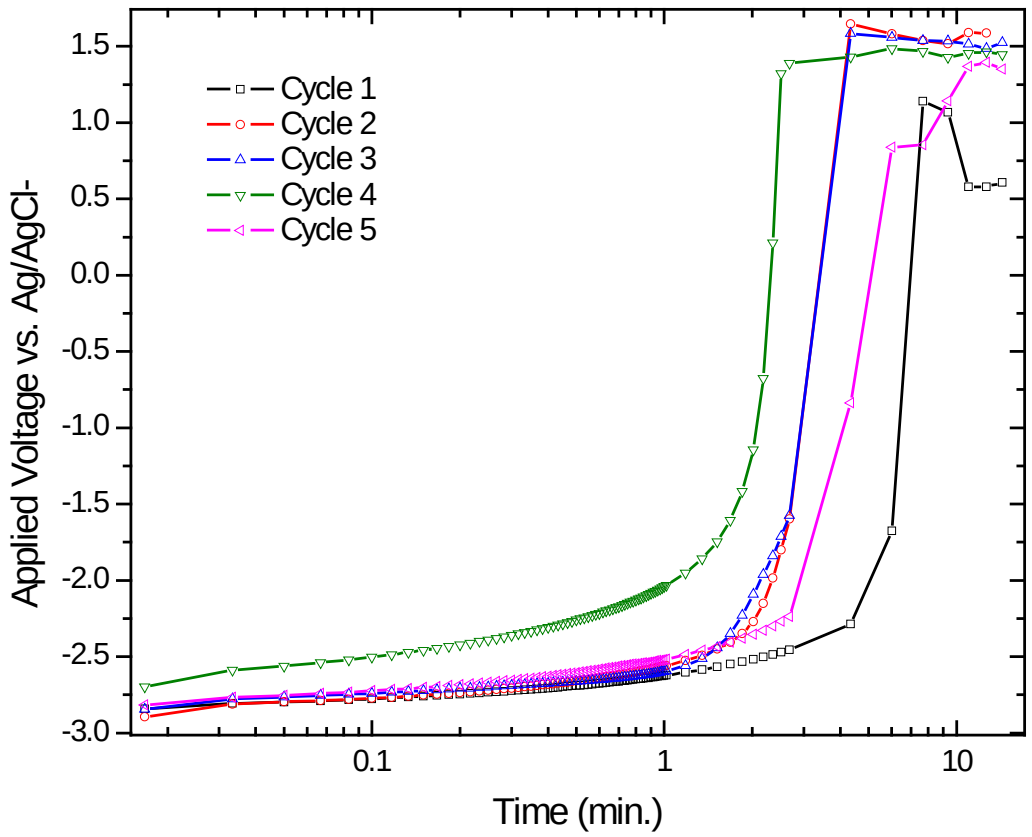

Figure 5.19: Chronopotentiometry voltage versus time plots used for charging the *a*-Si at the rate of 150 µA cm^{-2}. The data was taken with the decimate(log scale) option enabled giving fewer points later in the measurement.

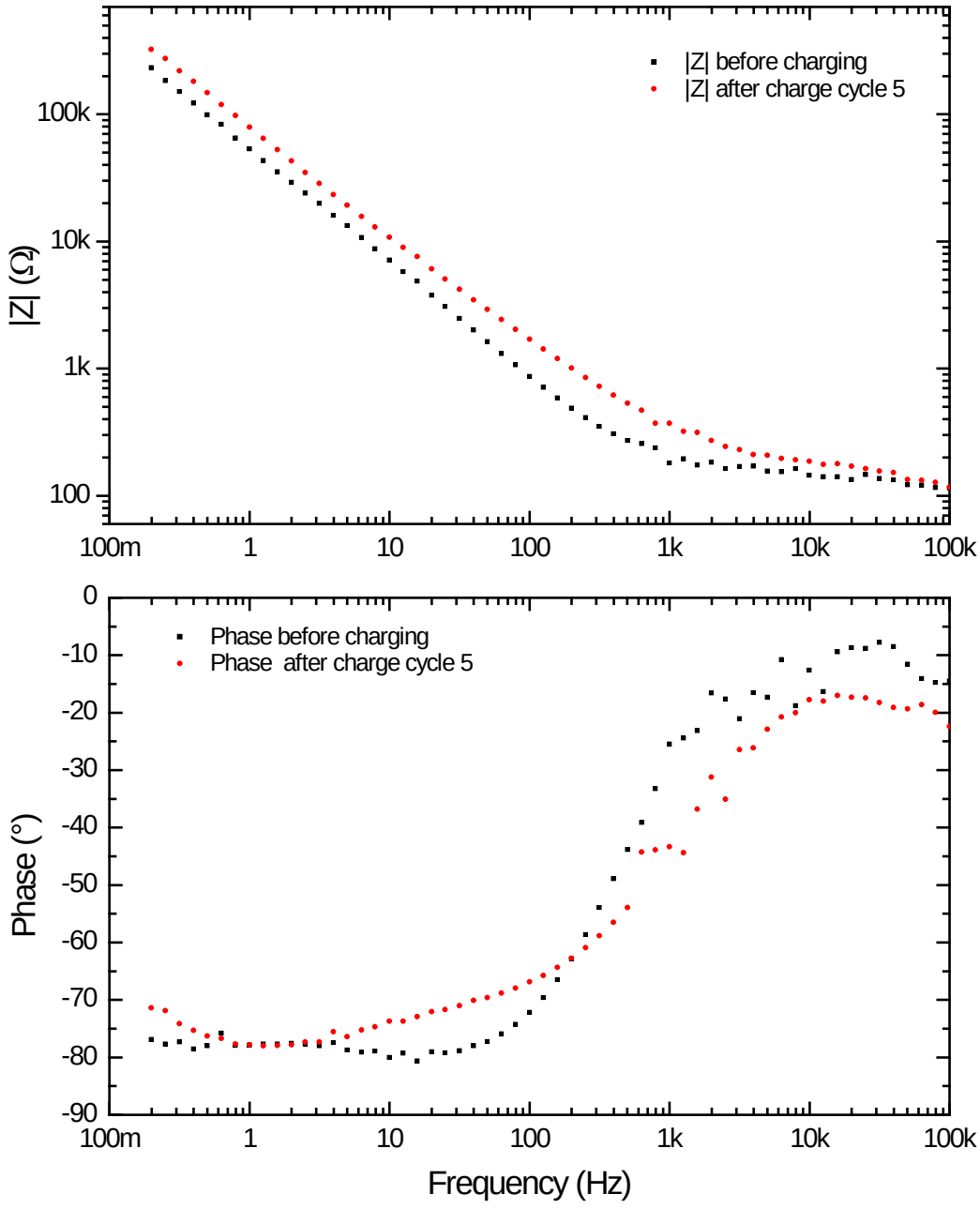

Figure 5.20: Bode plots of EIS measurements taken before and after Li intercalation using an AC signal of 10 mV rms while at 0 V DC cell potential. Bode plots after each charging cycle of the *a*-Si and taken in the spectral range of 200 mHz to100 kHz.

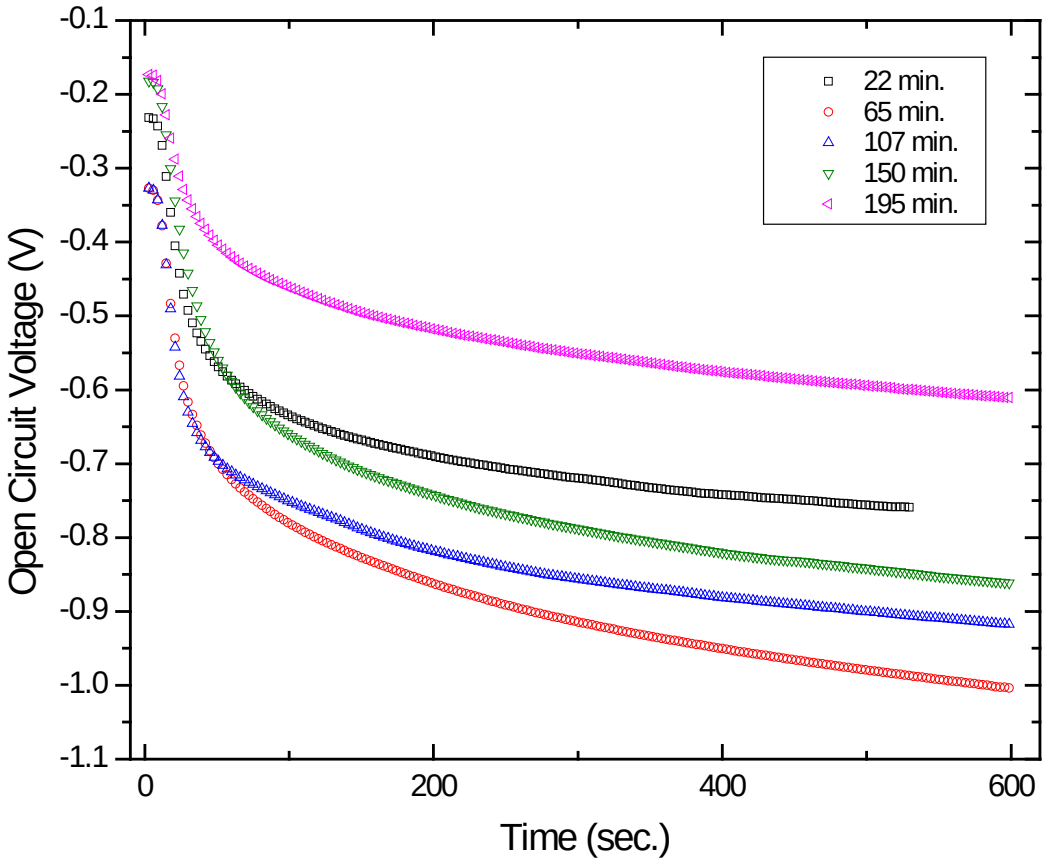

Figure 5.21: Open circuit potential scans after charging the *a*-Si at the rate of $150\,\mu A\,cm^{-2}$ used to discharge the samples.

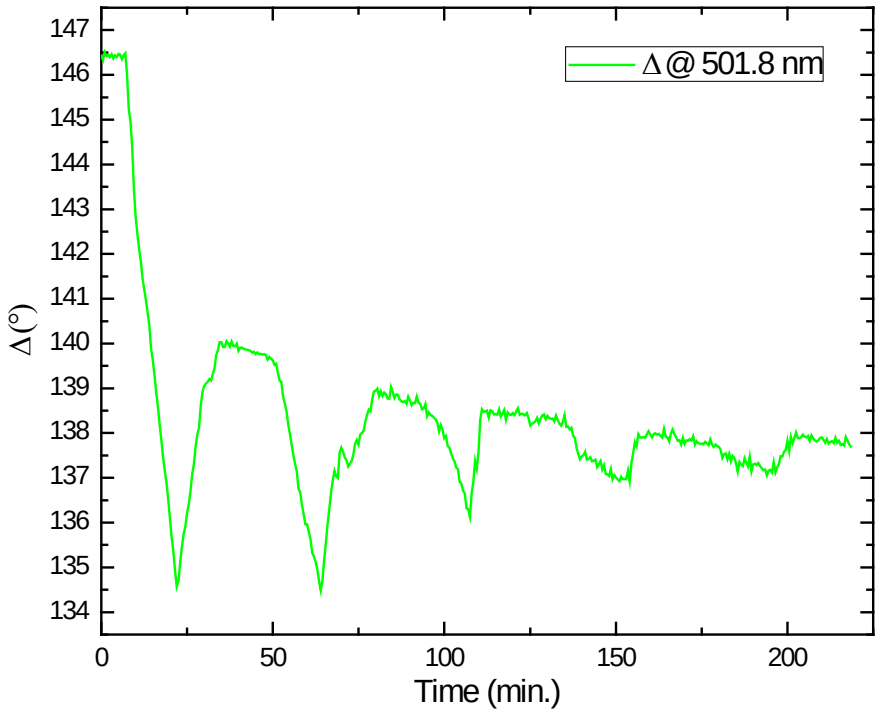

Figure 5.22: Measured Dynamic Δ data at the wavelength of 501.8 nm for Li intercalation into a-Si.

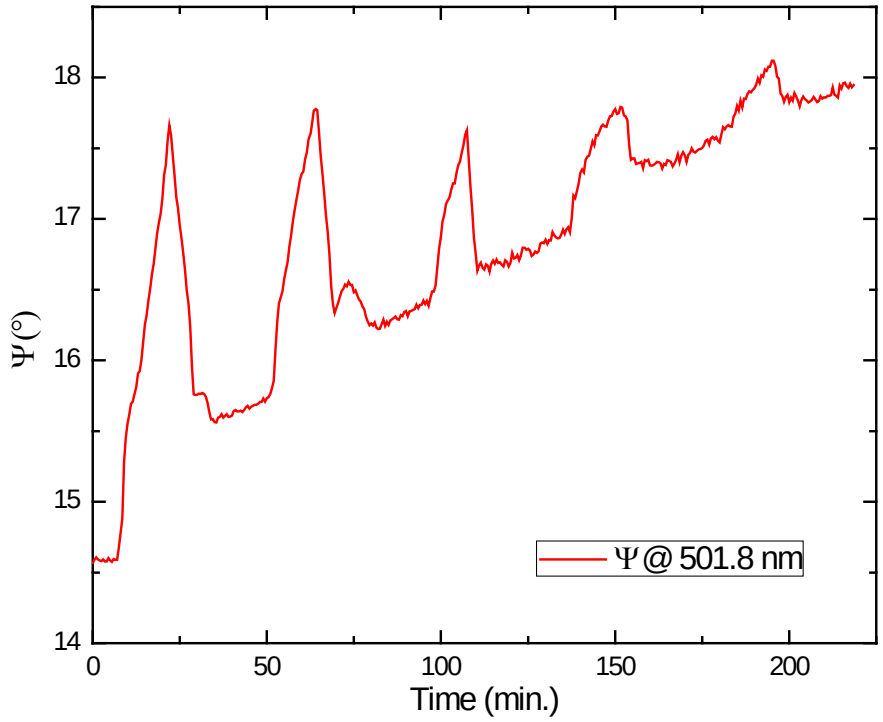

Figure 5.23: Measured Dynamic Ψ data at the wavelength of 501.8 nm for Li intercalation into *a*-Si.

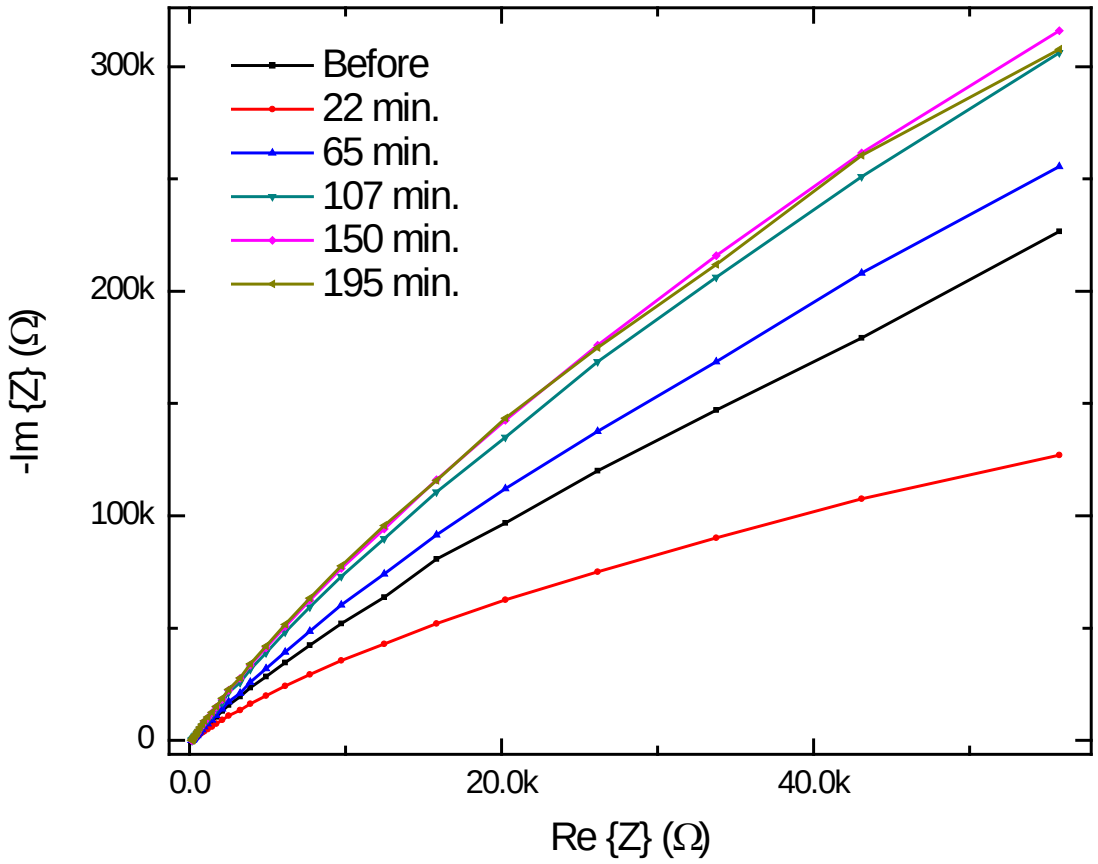

Figure 5.24: Nyquist plots after each charging cycle of the *a*-Si.

Chapter 6

Conclusions

Combined in-situ electrochemical impedance spectroscopy and spectroscopic ellipsometry are presented as a technique for analyzing film growth and intercalation. Combining the two techniques can give insight into the chemical, electrical and optical properties for real time characterization.

Anodically grown silicon dioxide was successfully characterized using both techniques. Both electrical and optical models had very good agreement between EIS capacitor model thickness and spectroscopic SE thickness models. The anodically grown SiO_2 according to both measurement techniques appears to be close in quality to thermally grown SiO_2, which has been a challenge for many researchers in the past. It is possible that the low current cyclic growth helps keep the chemical process from trapping oxygen, which forms pockets in the films that have plagued the use of anodically grown SiO_2 in semiconductor devices.

The Lithium intercalation experiments showed changes in the optical properties of both crystalline and amorphous silicon. The changes were not fully quantified, it is possible that the Li was plating onto the crystalline Si and not intercalating. In future work one can cap the cell to allow for an inert environment

of a noble gas, most likely argon, to allow for the use of lithium foil. Lithium foil can be used as a reference electrode and counter electrode to provide the Li-ion's that will flow from the CE (Li foil) to the WE (Si). Upon de-intercalation the Li-ions can then be rejoined to the Li foil.

The simulations in section 3.2 using the AB-EMA model show that the Mueller matrix elements should show large changes upon Li-ion intercalation in highly ordered nano-structured films, therefore, this technique may provide more insight into the stress induced in the silicon lattice during the Li-ion intercalation process and should be investigated further.

In summery, the anodically grown SiO_2 shows that it forms a uniform thin layer with optical properties similar to that of thermally grown SiO_2, with further study exact parameters for in-situ growth control could be established. However, the Li-ion intercalation data reveals that it cannot be analyzed as a uniform thin film and further studies and development of appropriate models and experimental parameters need to be performed.

Appendix A

Definitions

Anode is an electrode where oxidation takes place.

Cathode is an electrode where reduction.

Coulombic efficiency is the efficiency with which charge is transferred in a system facilitating an electrochemical reaction.

Current collector is the metal contact connecting the anode or cathode to an external circuit.

Deintercalation is the expulsion of a foreign atom from some crystal lattice where it has been residing (usually in interstitial spaces).

Electrode is a conductor used to establish electrical contact with a nonmetallic part of a circuit such as an electrolyte.

Electrochemistry is defined as the branch of chemistry that deals with oxidation-reduction reactions that transfer electrons to form electrical energy rather

than heat energy. Both the cathode and anode together make up an electrochemical cell.

Electrolysis is the passage of a direct electric current through an ionic substance that is either molten or dissolved in a suitable solvent, resulting in chemical reactions at the electrodes and separation of materials.

Electrolyte is any substance containing free ions that make the substance electrically conductive.

Energy Density is a term used for the amount of energy stored in a given system or region of space per unit volume.

Faradaic is charge transferred across the electrified interface as a result of an electrochemical reaction.

Intercalation is the incorporation of a foreign atom into some crystal lattice (usually in the interstitial spaces).

Interstitial in a crystalline solid, an atom that is not located on a lattice site.

Non-faradaic is the charge associated with movement of electrolyte ions, reorientation of solvent dipoles, adsorption/desorption, etc. at the electrode-electrolyte interface. This is the background current in voltammetry measurements.

Oxidation is the loss of electrons or an increase in oxidation state by a molecule, atom, or ion.

Power density is the amount of power (time rate of energy transfer) per unit volume

Primary cell is any kind of battery in which the electrochemical reaction is not reversible, rendering the cell non-rechargeable.

Reduction(reactivity) is the gain of electrons or a decrease in oxidation state by a molecule, atom, or ion.

Secondary cell is a rechargeable battery or storage battery is a group of one or more electrochemical cells. They are known as secondary cells because their electrochemical reactions are electrically reversible.

Redox are reactions that describe all chemical reactions in which atoms have their oxidation number changed.

References

[1] A. Bard and L. Faulkner, *Electrochemical methods: fundamentals and applications* (Wiley, 2001), ISBN 9780471043720, URL http://books.google.com/books?id=kv56QgAACAAJ. v, viii, 32, 33, 34, 35, 36, 38

[2] B. A. Boukamp, G. C. Lesh, and R. A. Huggins, Journal of The Electrochemical Society **128**, 725 (1981), URL http://link.aip.org/link/?JES/128/725/1. viii, 14, 15

[3] U. Kasavajjula, C. Wang, and A. J. Appleby, Journal of Power Sources **163**, 1003 (2007), ISSN 0378-7753, selected Papers presented at the FUEL PROCESSING FOR HYDROGEN PRODUCTION SYMPOSIUM at the 230th American Chemical SocietyNational Meeting Washington, DC, USA, 28 August - 1 September 2005, URL http://www.sciencedirect.com/science/article/pii/S037877530602026X. viii, 2, 14, 15, 72

[4] A. Patil, V. Patil, D. Wook Shin, J.-W. Choi, D.-S. Paik, and S.-J. Yoon, Materials Research Bulletin **43**, 1913 (2008), ISSN 0025-5408, URL http://www.sciencedirect.com/science/article/pii/S0025540807003868. 3, 4, 72

[5] J. Tarascon and M. Armand, Nature **414**, 359 (2001), ISSN 0028-0836, URL http://dx.doi.org/10.1038/35104644. 7

[6] H. Physics, *Abundances of the elements in the earth's crust*, http://hyperphysics.phy-astr.gsu.edu/hbase/tables/elabund.html (2011), hyper Physics. 8

[7] W. C. O'Mara, *Handbook of Semiconductor Silicon Technology* (William Andrew Inc., 1990). 8

[8] R. Krebs, *The history and use of our earth's chemical elements: a reference guide* (Greenwood Press, 1998), ISBN 9780313301230. 8, 9

[9] M. Silberberg, *Chemistry: the molecular nature of matter and change* (McGraw-Hill, 2002), ISBN 9780072475807. 13

[10] H. Fujiwara, *Spectroscopic ellipsometry: principles and applications* (John Wiley & Sons, 2007), ISBN 9780470016084, URL http://books.google.com/books?id=fPOQynOwXX4C. 17, 19

[11] M. Schubert, *Infrared Ellipsometry on Semiconductor Layer Structures Phonons, Plasmons, and Polaritons* (Springer, 2005). 19, 23, 24

[12] D. Schmidt, Ph.D. thesis, University of Nebraska - Lincoln (2010). 20, 22, 29

[13] R. Azzam and N. Bashara, *Ellipsometry and polarized light*, North-Holland personal library (Elsevier, 1999), ISBN 9780444870162, URL http://books.google.com/books?id=_vlozgAACAAJ. 21

[14] M. Bass, *Handbook of optics* (McGraw-Hill, 2010). 21, 22

[15] M. Schubert and W. Dollase, Opt. Lett. **27**, 2073 (2002), URL http://ol.osa.org/abstract.cfm?URI=ol-27-23-2073. 22

[16] H. Tompkins and E. Irene, *Handbook of ellipsometry* (William Andrew Pub., 2005), ISBN 9783540222934, URL http://books.google.com/books?id=xX9qJfqBttQC. 22

[17] M. F. Saenger, Master's thesis, University of Leipzig Faculty of Physics and Geosciences (2006). 25

[18] E. Palik, G. Ghosh, and K. (Firm), *Handbook of optical constants of solids: five-volume set*, no. v. 4 in Handbook of Optical Constants of Solids (Academic Press, 1998), ISBN 9780125444231, URL http://books.google.com/books?id=VpuVttd2cuEC. 29

[19] M. Rasigni and G. Rasigni, J. Opt. Soc. Am. **67**, 54 (1977), URL http://www.opticsinfobase.org/abstract.cfm?URI=josa-67-1-54. 29

[20] P. P. David Loveday and B. Rodgers, JCT CoatingsTech pp. 46–52 (2004). 39, 41

[21] M. Orazem and B. Tribollet, *Electrochemical impedance spectroscopy*, The Electrochemical Society series (Wiley, 2008), ISBN 9780470041406, URL http://books.google.com/books?id=buSd3wVBQfkC. 40

[22] A. Andreas Arie, W. Chang, and J. Kee Lee, Journal of Electroceramics **24**, 308 (2010-06-01), ISSN 1385-3449, URL http://dx.doi.org/10.1007/s10832-009-9573-z.

[23] A. Andreas Arie, W. Chang, and J. Kee Lee, Journal of Electroceramics **24**, 308 (2010), ISSN 1385-3449, 10.1007/s10832-009-9573-z, URL http://dx.doi.org/10.1007/s10832-009-9573-z.

[24] T. Berlind, G. K. Pribil, D. Thompson, J. A. Woollam, and H. Arwin, physica status solidi (c) **5**, 1249 (2008), ISSN 1610-1642, URL http://dx.doi.org/10.1002/pssc.200777897. 50, 52

[25] C. K. Chan, H. Peng, G. Liu, K. McIlwrath, X. F. Zhang, R. A. Huggins, and Y. Cui, Nat Nano **3**, 31 (2008), ISSN 1748-3387, URL http://dx.doi.org/10.1038/nnano.2007.411.

[26] J. Cho, J. Mater. Chem. **20**, 4009 (2010), ISSN 0959-9428, URL http://dx.doi.org/10.1039/B923002E.

[27] M.-W. O. Dictionary (Retrieved 25 June 2011), URL http://www.merriam-webster.com/dictionary/battery.

[28] M. Doyle, J. Newman, and J. Reimers, Journal of Power Sources **52**, 211 (1994), ISSN 0378-7753, URL http://www.sciencedirect.com/science/article/pii/0378775394020124.

[29] X. Gao, J. Hale, S. Heckens, and J. A. Woollam, Journal of Vacuum Science & Technology A: Vacuum, Surfaces, and Films **16**, 429 (1998), URL http://link.aip.org/link/?JVA/16/429/1.

[30] P. Gray, P. Hurst, S. Lewis, and R. Meyer, *Analysis and design of analog integrated circuits* (Wiley, 2009), URL http://books.google.com/books?id=VBB4QAAACAAJ. 62

[31] J. Guo, A. Sun, X. Chen, C. Wang, and A. Manivannan, Electrochimica Acta **56**, 3981 (2011), ISSN 0013-4686, URL http://www.sciencedirect.com/science/article/pii/S0013468611002258.

[32] A. Hamnett, J. Chem. Soc., Faraday Trans. **89**, 1593 (1993), URL http://dx.doi.org/10.1039/FT9938901593.

[33] W. A. M. Harland G. Tompkins, *Spectroscopic Ellipsometry and Reflectometry: A User's Guide* (John Wiley & Sons, Inc., 1999).

[34] C. M. Herzinger, B. Johs, W. A. McGahan, J. A. Woollam, and W. Paulson, Journal of Applied Physics **83**, 3323 (1998), URL http://link.aip.org/link/?JAP/83/3323/1. 51, 59

[35] G. E. Jellison and Jr., Thin Solid Films **313-314**, 33 (1998), ISSN 0040-6090.

[36] H. Jung, M. Park, Y.-G. Yoon, G.-B. Kim, and S.-K. Joo, Journal of Power Sources **115**, 346 (2003), ISSN 0378-7753, URL http://www.sciencedirect.com/science/article/pii/S0378775302007073.

[37] H. Kim, B. Han, J. Choo, and J. Cho, Angewandte Chemie International Edition **47**, 10151 (2008), ISSN 1521-3773, URL http://dx.doi.org/10.1002/anie.200804355.

[38] T. L. Kulova, A. M. Skundin, Y. V. Pleskov, O. I. Konkov, E. I. Terukov, and I. N. Trapeznikova, Semiconductors **40**, 468 (2006-04-11), ISSN 1063-7826, URL http://dx.doi.org/10.1134/S1063782606040178. 72

[39] J. Li and J. R. Dahn, Journal of The Electrochemical Society **154**, A156 (2007), URL http://link.aip.org/link/?JES/154/A156/1. 72

[40] K. Peng, J. Jie, W. Zhang, and S.-T. Lee, Appl. Phys. Lett. **93**, 033105 (2008), URL http://link.aip.org/link/?APL/93/033105/1.

[41] E. Pollak, G. Salitra, V. Baranchugov, and D. Aurbach, The Journal of Physical Chemistry C **111**, 11437 (2007), ISSN 1932-7447, URL http://dx.doi.org/10.1021/jp0729563.

[42] R. Ruffo, S. S. Hong, C. K. Chan, R. A. Huggins, and Y. Cui, The Journal of Physical Chemistry C **113**, 11390 (2009), ISSN 1932-7447, URL http://dx.doi.org/10.1021/jp901594g.

[43] P. Schmuki, H. Bohni, and J. A. Bardwell, Journal of The Electrochemical Society **142**, 1705 (1995), URL http://link.aip.org/link/?JES/142/1705/1.

[44] V. A. Sethuraman, K. Kowolik, and V. Srinivasan, Journal of Power Sources **196**, 393 (2011), ISSN 0378-7753, URL http://www.sciencedirect.com/science/article/pii/S0378775310010293.

[45] D. E. Smith, Analytical Chemistry **36**, 962 (1964), http://pubs.acs.org/doi/pdf/10.1021/ac60212a007, URL http://pubs.acs.org/doi/abs/10.1021/ac60212a007.

[46] R. Teki, M. K. Datta, R. Krishnan, T. C. Parker, T.-M. Lu, P. N. Kumta, and N. Koratkar, Small **5**, 2236 (2009), ISSN 1613-6829, URL http://dx.doi.org/10.1002/smll.200900382.

[47] T. E. Tiwald, A. D. Miller, and J. A. Woollam, AIP Conference Proceedings **449**, 221 (1998), URL http://link.aip.org/link/?APC/449/221/1. 48

[48] M. Urbain, M. Hinaje, S. Rael, B. Davat, and P. Desprez, Energy Conversion, IEEE Transactions **25**, 862 (2010), ISSN 0885-8969.

[49] J. Wang, *Analytical Electrochemistry* (John Wiley & Sons, 1994), ISBN 9780471185734, URL http://books.google.com/books?id=hXFHPgAACAAJ.

[50] W. Wang and P. N. Kumta, ACS Nano **4**, 2233 (2010), ISSN 1936-0851, URL http://dx.doi.org/10.1021/nn901632g.

[51] J. Xiao, W. Xu, D. Wang, D. Choi, W. Wang, X. Li, G. L. Graff, J. Liu, and J.-G. Zhang, Journal of The Electrochemical Society **157**, A1047 (2010), URL http://dx.doi.org/10.1149/1.3464767.

[52] X. Xuan, J. Wang, J. Tang, G. Qu, and J. Lu, Spectrochimica Acta Part A: Molecular and Biomolecular Spectroscopy **56**, 2131 (2000), ISSN 1386-1425, URL http://www.sciencedirect.com/science/article/pii/S1386142500002675.

[53] L. L. Zhang and X. S. Zhao, Chem. Soc. Rev. **38**, 2520 (2009).

[54] (????).